

# Enhancement of Light via Surface Plasmon Coupling in the Visible

Emily A. Ray

A dissertation submitted to the faculty of the University of North Carolina at Chapel Hill in partial fulfillment of the requirements for the degree of Doctor of Philosophy in the Department of Physics and Astronomy.

Chapel Hill  
2012

Approved by:

Rene Lopez

Charles E. Evans

Christopher J. Fecko

Laurie E. McNeil

Edward T. Samulski

## ABSTRACT

**Emily A. Ray: Enhancement of Light via Surface Plasmon Coupling in the Visible  
(Under the direction of Rene Lopez)**

The incidence of light with momentum components outside the light cone on the surface of a negative permittivity material results in the excitation of a surface plasmon polariton and the enhancement of the incident signal when there is momentum and energy conservation. This process has an impact across many fields including imaging, optical computing, signaling, and photovoltaic devices, among others. I examine the role and tunability of light-surface plasmon interactions in several applications. I demonstrate a tuned metamaterial grating system that allows the signal from evanescent waves to be detected in the far field in the visible regime. I fabricate a metamaterial that is tuned to support surface plasmons that couple to visible light across a wide range of wavelengths. I characterize the plasmonic response through a simple technique wherein a the reflection from a subwavelength grating on a metamaterial indicates surface plasmon coupling when its intensity dips. With this I demonstrate that the reflection trends match well with simulation, indicating that coupling of light to surface plasmons occurs at the expected crossing points. The strength of coupling (denoted by the drop in reflection) however, is less than expected. Transmission measurements reveal a depolarizing effect that accounts for the decrease in evanescent light enhancement by the surface plasmons and is

due to the surface roughness at the interfaces between the metal and dielectric. I also use a tuned metamaterial perforated with a subwavelength array of circular apertures to exhibit extraordinary transmission in the visible. I compare the transmission of the metamaterial to that of a thin film of Ag with equivalent thickness that has fewer plasmon modes and a resonance position in the UV to find that for 400 nm, both thin films exhibit a transmission minimum at 650 nm. Both film spectra have plasmon-aided extraordinary transmission peaks where there is momentum and energy conservation between the evanescent waves produced by the diffraction grating and the surface plasmons in the metamaterial at 570 nm and 700 nm. Here, more light is transmitted through the holes than is incident on them. Furthermore, I see that the surface plasmon generation by the holes themselves is negligible compared to those generated by the surface plasmon. I then explore the mechanism of increased external quantum efficiency with plasmonic structures in organic bulk heterojunction solar cells. I build an inverted bulk heterojunction solar cell with a Ag back cathode patterned with a diffraction grating to separate the possible mechanisms of enhanced current production. I-V curves from the patterned cell signify a total efficiency 3 times larger than a flat reference cell and the incident photon to electron conversion efficiency exhibits peaks where there is an increase in interaction path length of the incident light in the active layer due to scattering and none at the surface plasmon resonance position leading to the conclusion that the increase in performance is due to scattering and not plasmon generation.

## ACKNOWLEDGMENTS

They say it takes a village to raise a child. The same is true for a scientist. Only the village is spread across the map and time and is littered with broken toys, duct tape, hot glue, and “borrowed” equipment. There is no way I would be in this position today without my village, and I would like to take this opportunity to thank them for their contributions to my growth as a researcher. First and foremost, I must thank my graduate advisor, Rene Lopez. He was the one who taught me that a broken filter really meant that you now had two filters, steered me along a productive path, provided insight, taught me to think about physics while I was doing it, and overlooked the fact that I was late to every meeting we ever scheduled. Rene, thank you. To my committee, I cannot say enough how much I appreciate the time that you have given me out of your busy schedules, and the insight into your research when I have been confused.

I owe a great deal to my professional collaborators who made my research as smooth and quick as possible. Meredith Hampton, who optimized countless samples, and Evgenii Donev who simulated the extraordinary optical transmission through the films I made.

My laboratory colleagues and postdocs who were responsible for passing on a great deal of information, tricks, insight, process recipes, and extra hands: John Tumbleston, Kristen Alexander, Rudresh Ghosh, Yingchi Liu, Abay Dinku, Yukihiro Hara, Hong Nguyen, Shota Kita, and Kejiro Suzuki. I would be remiss if I did not include those around me

who formed the network of borrowed chemicals, equipment, and outsourced knowledge that supports the scientific community. Superfine lab, you know who you are.

Finally, I would like to thank my mentors who taught me physics, shaped the way I think about science, and imparted on me the invaluable set of experimental skills and tricks that exists nowhere in any textbook. Thank you to Pat Bunton, Richard Haglung, Stephen Lewis, John Rozen, Leonard Feldman, Toshihiko Baba, and Rene Lopez.

## TABLE OF CONTENTS

ABSTRACT . . . . .	ii
ACKNOWLEDGEMENTS . . . . .	iv
LIST OF TABLES . . . . .	ix
LIST OF FIGURES . . . . .	x
LIST OF ABBREVIATIONS . . . . .	xiii
1 INTRODUCTION . . . . .	1
1.1 Overview . . . . .	1
1.2 The Electromagnetic Wave . . . . .	3
1.3 Fourier Space . . . . .	6
1.4 The Light Cone . . . . .	8
1.5 Imaging . . . . .	11
1.6 Surface Plasmons . . . . .	12
1.7 Coupling . . . . .	14
1.7.1 Evanescent Wave Productions . . . . .	14
1.7.2 Plasmonic Grating Coupling . . . . .	15
1.8 Metamaterials . . . . .	16

2	CREATION AND DETECTION OF ENHANCED EVANESCENT WAVES IN THE FAR-FIELD . . . . .	24
2.1	The Ideal Superlens . . . . .	26
2.2	Fabrication . . . . .	30
2.3	Experiment and Simulation . . . . .	32
2.4	Conclusions . . . . .	36
3	NUMERICAL DESIGN AND SCATTERING LOSSES OF A 1D METALLO- DIELECTRIC MULTILAYER WITH BROADBAND COUPLING OF PROP- AGATING WAVES TO PLASMON MODES IN THE VISIBLE RANGE . . .	37
3.1	Simulation and Fabrication . . . . .	40
3.2	Experimental . . . . .	44
3.3	Conclusions . . . . .	48
4	CHARACTERIZATION OF TRANSMISSION SPECTRA THROUGH A METALLO- DIELECTRIC METAMATERIAL THIN FILM PERFORATED BY SUBWAVE- LENGTH CIRCULAR HOLE ARRAYS . . . . .	50
4.1	Fabrication and Spectral Response . . . . .	56
4.2	Experiment and Simulation . . . . .	58
4.3	Conclusions . . . . .	64
5	PLASMON MEDIATED ABSORPTION IN ORGANIC BULK HETEROJUNC- TION SOLAR CELLS . . . . .	65
5.1	Fabrication . . . . .	69

5.2	Electrical Characterization . . . . .	70
5.3	Plasmonic Isolation . . . . .	72
5.4	Scattering . . . . .	74
5.5	Conclusions . . . . .	76
A	RECIPES . . . . .	78
B	POLARIZATION STUDIES THROUGH VARIOUS METAMATERIAL CON- FIGURATIONS . . . . .	84
C	EXPERIMENTAL SET-UPS . . . . .	88
	BIBLIOGRAPHY . . . . .	93

## LIST OF TABLES

4.1	Experimental Absolute Transmission Efficiency . . . . .	64
A.1	Ion beam milling of Ag . . . . .	81
A.2	Ion beam milling of 4 pair MM . . . . .	82
A.3	PMMA Spincoating curves from Meredith Hampton . . . . .	83
A.4	950k PMMA Spincoating curves . . . . .	83
A.5	495k PMMA Spincoating curves . . . . .	83

## LIST OF FIGURES

1.1	Electromagnetic wave . . . . .	4
1.2	Plane of incidence . . . . .	5
1.3	Fourier transform of an infinitely periodic structure . . . . .	6
1.4	Fourier transform of single apertures with increasing diameter . . . . .	7
1.5	Fourier transform convolution single aperture periodicity . . . . .	9
1.6	Dispersion relation of the light cone in vacuum . . . . .	10
1.7	Surface plasmon dispersion . . . . .	14
1.8	Momentum exchange between light and a plasmonic diffraction grating . . . . .	17
1.9	Effect of film thickness ratio variation on permittivity tensor . . . . .	18
1.10	Surface plasmon dispersion at two interfaces . . . . .	19
1.11	Dependence of metamaterial resonance on film thickness variation . . . . .	20
1.12	Tikhodeev matrix method visualization . . . . .	22
2.1	Light transmitted and reflected through a $n=-1$ superlens . . . . .	27
2.2	Metamaterial cross section . . . . .	31
2.3	Kretschman-Raether schematic . . . . .	33
2.4	Metamaterial dispersion curves Kretschman-Raether . . . . .	34
2.5	TM transmission Kretschman-Raether . . . . .	35
2.6	TE transmission Kretschman-Raether . . . . .	35

3.1	Visible transmission vs. momentum for a metamaterial . . . . .	40
3.2	Dispersion curve of a 10 pair Ag-Al <sub>2</sub> O <sub>3</sub> Metamaterial . . . . .	41
3.3	Reflection and transmission comparison of artificial and real long k-vector generators on a metamaterial . . . . .	42
3.4	10 pair Ag-Al <sub>2</sub> O <sub>3</sub> metamaterial cross section with diffraction grating . . . . .	44
3.5	Reflection from a 10 pair Ag-Al <sub>2</sub> O <sub>3</sub> metamaterial with a plasmonic diffraction grating . . . . .	46
3.6	Cross polarization measurements through a 10 pair Ag-Al <sub>2</sub> O <sub>3</sub> metamaterial	47
3.7	Transmission microscope in confocal configuration . . . . .	48
4.1	Dispersion curve of a 4-pair Ag-Al <sub>2</sub> O <sub>3</sub> metamaterial . . . . .	52
4.2	Spectral response of metamaterial, Ag, and 180 nm diameter hole . . . . .	53
4.3	Periodic hole arrays and a metamaterial cross section . . . . .	54
4.4	Experimental and simulated transmission vs. wavelength plots for varying hole diameters in a metamaterial and a Ag thin film. . . . .	59
4.5	Schematic of a transmission microscope in confocal configuration . . . . .	60
4.6	The absolute transmission efficiency for a metamaterial . . . . .	63
5.1	Schematic of the functioning of a solar cell . . . . .	67
5.2	Graphical model of the patterned inverted solar cell. . . . .	69
5.3	Solar cell fabrication process . . . . .	70
5.4	I-V curves for a patterned and flat reference cell. . . . .	71
5.5	P3HT:PCBM-Ag plasmon dispersion curve . . . . .	72
5.6	Maximum-Normalized IPCE curves for a patterned and reference cell. . . . .	73

5.7	Experimental maximum-normalized IPCE vs. wavelength for varying incident angles. . . . .	74
5.8	Simulated optical absorption of a patterned solar cell as a function of incident angle . . . . .	75
5.9	Solar cell diffraction schematic . . . . .	76
5.10	Path length change due to diffraction through P3HT:PCBM by a 400 nm periodicity grating . . . . .	77
B.1	Polarization and interference schematic . . . . .	84
B.2	Transmission Enhancement . . . . .	85
B.3	Cross polarization in various configuration . . . . .	86
B.4	Cross polarization measurements through a 10 pair Ag-Al <sub>2</sub> O <sub>3</sub> metamaterial . . . . .	87
C.1	Schematic of the Kretschman-Raether configuration . . . . .	89
C.2	Schematic of the interference microscope . . . . .	90
C.3	Schematic of a microscope in a confocal-like configuration . . . . .	91
C.4	Photograph of IPCE for varying incident angle set-up . . . . .	92

## LIST OF ABBREVIATIONS

<b>ATE</b>	Absolute Transmission Efficiency
<b>BHJ</b>	Bulk Heterojunction
<b>CW</b>	Continuous Wave
<b>DI</b>	Deionized
<b>EOT</b>	Extraordinary Optical Transmission
<b>FDTD</b>	Finite-Difference Time-Domain
<b>FSL</b>	Far-Field Superlens
<b>HOMO</b>	Highest Occupied Molecular Orbital
<b>IPA</b>	Isopropyl Alcohol
<b>IPCE</b>	Incident Photon-to-electron Conversion Efficiency
<b><math>J_{SC}</math></b>	Short Circuit Current
<b>LUMO</b>	Lowest Unoccupied Molecular Orbital
<b>P3HT:PCBM</b>	Poly(3-hexylthiophene:[6,6]-phenyl C61-butyric acid methylester)
<b>PFPE</b>	Perfluoropolyether
<b>PLD</b>	Pulsed Laser Deposition
<b>PMMA</b>	Poly(methyl methacrylate)
<b>PRINT</b>	Pattern Replication In Nonwetting Templates <sup>®</sup>
<b>TE</b>	Transverse Electric
<b>TM</b>	Transverse Magnetic
<b><math>V_{OC}</math></b>	Open Circuit Voltage

# CHAPTER 1

## INTRODUCTION

### 1.1 Overview

In this thesis I will explore the mechanisms and applications of the unique interactions between visible light and resonant surface plasmon polaritons that result in an enhanced signal. These couplings are brokered by subwavelength-periodicity plasmonic diffraction gratings and metamaterials with a negative refractive index and have effects in the fields of imaging, nanoscale fabrication, optical computing, and solar cells.

I begin with an introduction covering basic optics and the terminology used to describe surface plasmons. I will discuss briefly fourier transforms and momentum space, light to matter coupling, metamaterials, and the mathematical descriptions of surface plasmons, evanescent waves, and diffraction gratings. This will be followed by a description of the modeling program developed by our group used to simulate the plasmonic response of metamaterials.

In Chapter Two I explore an application of evanescent wave enhancement by surface plasmons, the far-field superlens (FSL) that is designed to image below the diffraction

limit. I will show that, with a metamaterial and evanescent waves generated from total internal reflection, the signal from non-propagating waves with large momentum components can be detected in the far field with standard optics. This experiment lays the foundation for building a FSL to form real time images with superresolution using visible incident light.

Chapter Three introduces a simple optical technique to characterize the plasmonic response of a metamaterial or thin film with the reflection from a single subwavelength grating. The reflection signal serves as a proxy for detection of evanescent waves in the far field and a structure in which it can be detected requires less materials processing than building a functional device to test the thin film for a superlens. It shows, crucially, a depolarizing scattering effect that occurs at the interfaces in the metamaterial where surface plasmon polaritons are generated.

Chapter Four explores an interesting side effect of a subwavelength hole array in a thin, negative permittivity film: extraordinary optical transmission (EOT), in which more light is transmitted through the holes than is incident on them due to light tunneling between the two interfaces with the aid of surface plasmons excited by the periodicity of the grating. I examine the behavior of a metamaterial as the negative permittivity thin film and compare the response to that of a Ag thin film. Despite the fact that the two have different dispersion relations, their transmission spectra are essentially the same due to higher order coupling to the dispersion modes and a common band gap.

Chapter Five illuminates the role of light-plasmon coupling in the enhanced electrical properties of a patterned inverted organic bulk heterojunction solar cell. I separate the

possible mechanisms of enhancement into light path length increase due to scattering and the increase in local electric field due to plasmon generation to determine the features that contribute to increased IPCE and reveal that while subwavelength structures can generate surface plasmons, they play no role in the increase of IPCE over a cell with no patterning.

Finally, a set of appendices will list some of the technical specifications useful in performing these experiments.

Appendix A contains thin film growth and nanoscale patterning recipes.

Appendix B shows the results of cross and parallel polarization measurements taken through various thin film and grating configurations.

Appendix C displays schematics and pictures of experimental set-ups built for the previous experiments.

## 1.2 The Electromagnetic Wave

I begin the discussion of light-surface plasmon interaction with an overview of the electromagnetic wave. It is a propagating oscillation of an electric and magnetic field. In this dissertation, I consider only the linearly polarized orientation where the electric and magnetic fields are confined to oscillate in fixed, mutually perpendicular planes that are transverse to the direction of propagation. This electromagnetic wave configuration is shown in Fig.1.1.

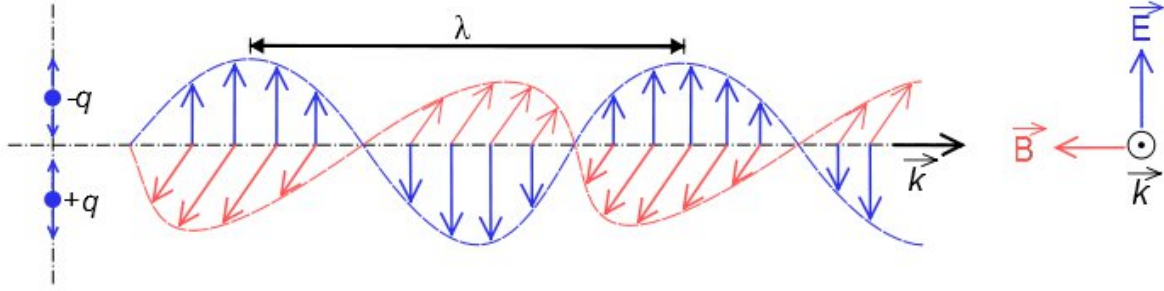


Figure 1.1: An illustration of an electromagnetic wave with a linear polarization of the electric (blue) and magnetic (red) fields(SuperManu, 2007).

The electric and magnetic field magnitudes are related by

$$E = vB \quad (1.1)$$

with  $v=c/n$ , where  $v$  is the speed of light in the medium of propagation,  $c$  is the speed of light in free space, and  $n$  is the refractive index of the propagating medium.

The electromagnetic wave is described by the maximum amplitude of the fields, ( $E_0$  or  $B_0$ ), the wavelength ( $\lambda$ ) which is the distance between two adjacent points of equal amplitude, the speed of propagation ( $v$ ), the momentum ( $k$ ) which is the fourier transform of the wavelength ( $2\pi/\lambda$ ) and points along the direction of propagation, and the frequency of oscillation ( $\omega$ ). Because the magnitude ratio of the fields is known and they are mutually perpendicular, only one field vector needs to be specified and the other can be determined. It is described by

$$\mathbf{E}(\mathbf{r}, \mathbf{t}) = \mathbf{E}_0 e^{i(\mathbf{k}\cdot\mathbf{r} - \omega t)} \quad (1.2)$$

where  $\mathbf{r}$  is the position, and  $t$  is the time.

When an electromagnetic wave interacts with an object or interface, the  $k$ -vectors

of the incident, reflected, and transmitted waves sweep out what is called the plane of incidence as illustrated in Fig.1.2. This provides the basis for the definition of polarization relating to an interface.

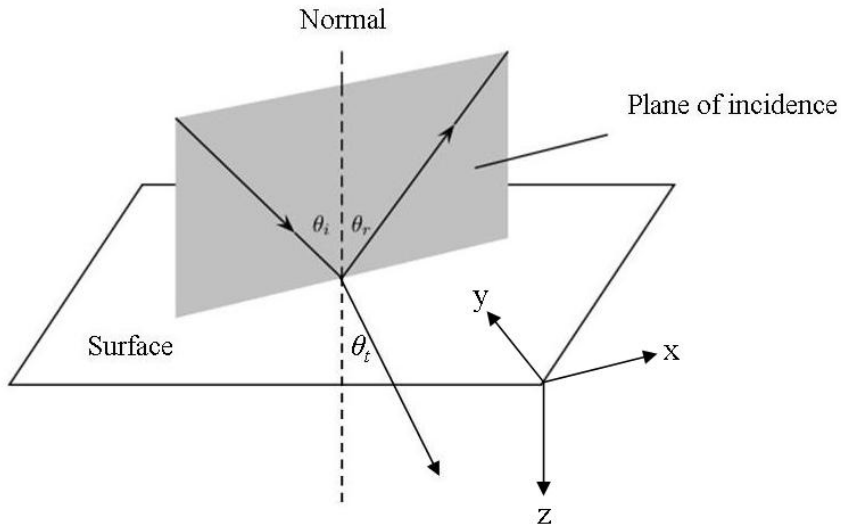


Figure 1.2: Illustration of the plane of incidence. Here  $\theta_i$ ,  $\theta_r$ , and  $\theta_t$  are the angle of the incident, reflected, and transmitted beams, respectively.

The orientation of the plane of incidence with respect to the electric and magnetic field vectors dictate the polarization of the light wave. For linearly polarized light, when the electric field oscillates parallel to the plane of incidence, it is called transverse magnetic (TM) polarized light. When the magnetic field oscillates parallel to the plane of incidence and the electric field transverse to that, it is called transverse electric (TE) polarized.

It is convenient to align the position axes along the plane of incidence. By convention, I choose the z-axis to be normal to the incident-transmitted interface in the plane of incidence and to be positive into the transmitted side. The x-axis is along the interface between the reflected and transmitted directions and the y-direction is perpendicular to

them to form a right handed coordinate system (Fig.1.2).

### 1.3 Fourier Space

In this thesis I will use the momentum to characterize the oscillations studied. Thus, it is necessary to discuss momentum space and the mathematical tool to convert between position (where units are measured in lengths) and momentum (where units are measured in inverse lengths). The fourier transform is defined with the following equation:

$$\hat{f}(k) = \int_{-\infty}^{+\infty} f(x)e^{-2\pi i x k} dx \tag{1.3}$$

where  $\hat{f}(k)$  is the inverse fourier transform. This is the tool that facilitates the conversion from a space to its reciprocal values.

Things that are extensive in position space, have small extent in momentum space, and things that are small in position space have a large value once they are transformed. When the fourier transform is applied to a light wave with an infinite set of oscillations separated by a distance  $\lambda$ , it produces the discrete value  $k=2\pi/\lambda$ . Fig.1.3 demonstrates this property.



Figure 1.3: Illustration of array of lines (left) and the corresponding two-dimensional fourier transform (right).

The transform of a single aperture will be crucial in describing the plasmons generated by a subwavelength diameter hole and a plasmonic grating that consists of an array of

these features. Fig.1.4 shows four circular single apertures with increasing diameter and their representation in momentum space. An aperture with small diameter in position space will have a large number of non-zero harmonics needed to describe the system in momentum space. This means that evanescent waves generated from a subwavelength aperture will have large magnitude momentum values compared to  $2\pi/\lambda$  as the hole is very small.

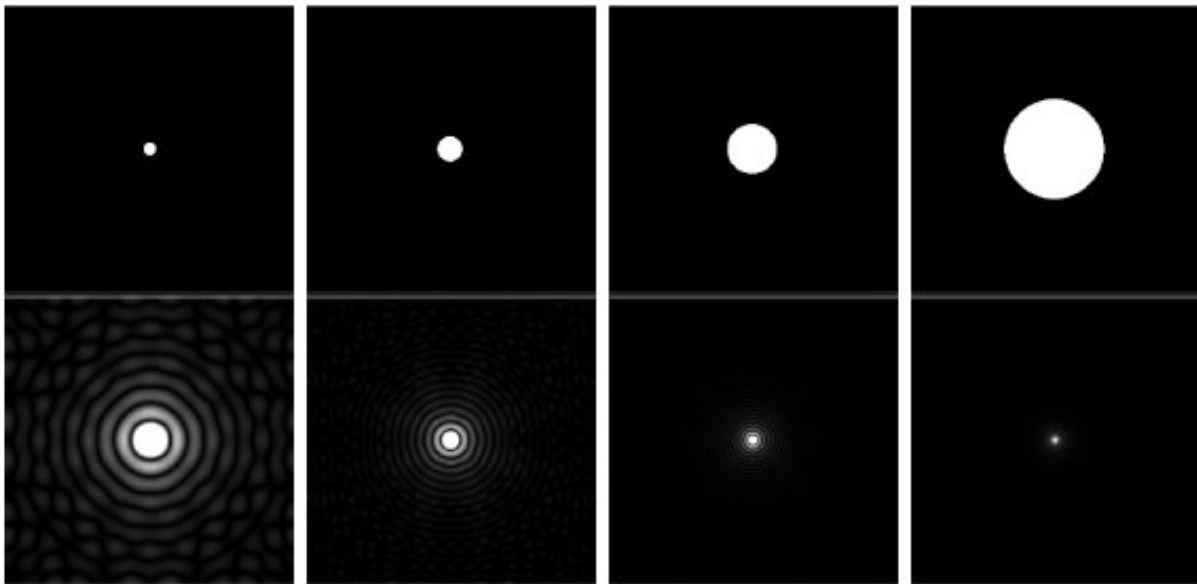


Figure 1.4: Illustration of circular apertures of different size (upper row) and their corresponding fourier transforms (lower row). The intensities are normalized to their respective maximum value.

The final feature of the fourier transform that I will explore is convolution. In the fourier transform, “convolution” and “product” are complementary mathematical terms. The fourier transform of a product of two functions is equal to the convolution of the fourier transforms of the two functions. The convolution is important in the application to real systems that cannot be described as either infinite or delta functions. For example, a two-dimensional diffraction grating can be made with a periodic array of circular apertures

of nonzero diameter. The description in momentum space is then the convolution of the fourier transform of a single aperture and a periodic array of delta functions. Fig.1.5 illustrates the effect of this convolution.

## 1.4 The Light Cone

For light to propagate to the far-field, the momentum value must be inside what is referred to as the light cone. It is defined by the speed in the propagating medium and is a curve swept out by the equation

$$c = \frac{\omega}{k} \quad (1.4)$$

in vacuum and

$$v = \frac{c}{n} = \frac{\omega}{nk} \quad (1.5)$$

for light in a medium with refractive index  $n$  where the speed of propagation is slowed through absorption and re-emission.

A simple way to visualize this restriction is with a dispersion graph in Fig.1.6. The slope of the line is  $1/c$ . Values below this line have small magnitude momentum vectors and are propagating. The area outside the light cone is exclusively light with momentum vectors larger than  $(k_0=2\pi/\lambda)$  and is called evanescent. Propagating light with momentum  $\leq k_0$  has a nonzero intensity in the far-field while evanescent waves decay outside the near-field because of imaginary  $k$ -vector components. It is common to decompose the

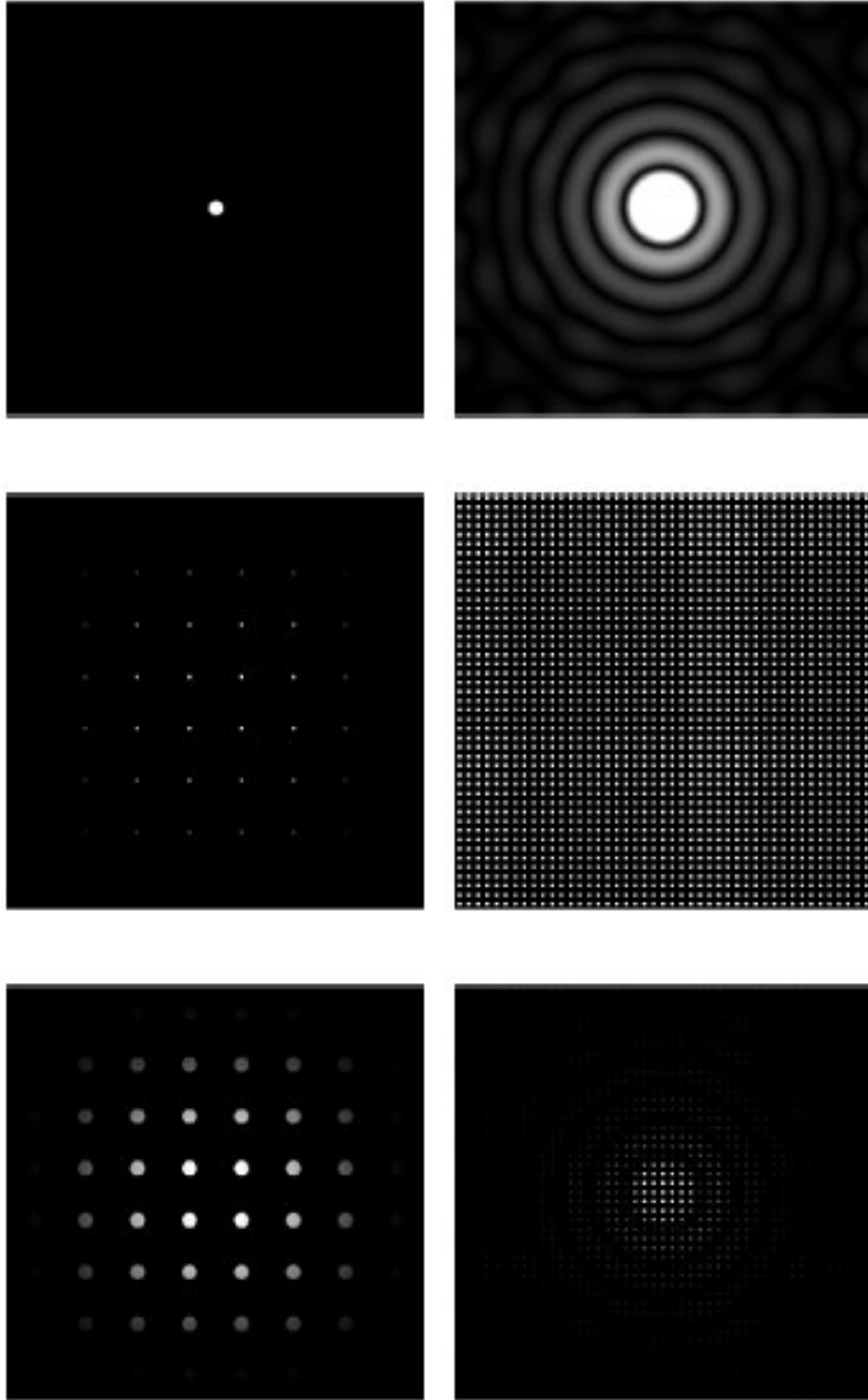


Figure 1.5: Illustration (top) a single aperture and its fourier transform, (middle) a periodic array of delta functions with a finite number of periods and its fourier transform, and (bottom) an periodic array of apertures with a finite number of periods and its fourier transform.

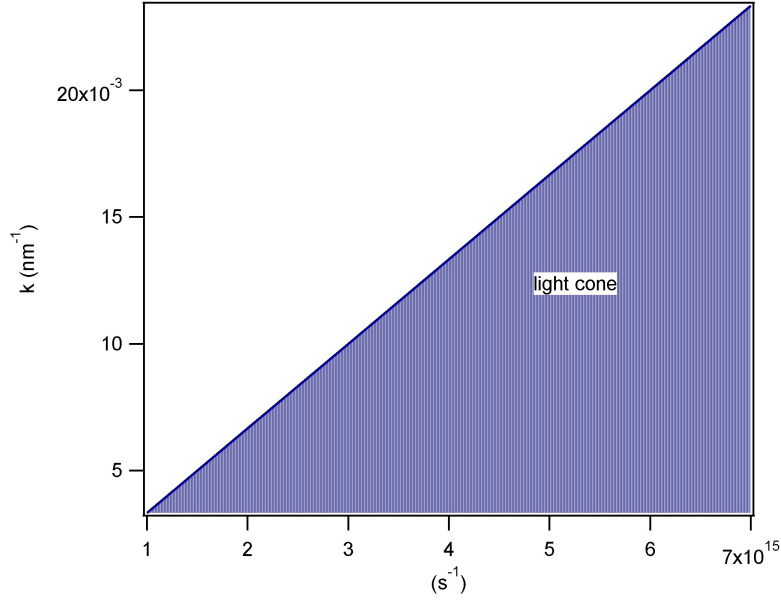


Figure 1.6: Graph of  $k$  vs.  $\omega$ , the dispersion relation of the light cone in vacuum bounded by  $c = \omega/k$ .

momentum vector into its components along the transverse and longitudinal directions.

$$\sqrt{k_T^2 + k_L^2} = k_0 = \sqrt{k_x^2 + k_y^2 + k_z^2} \quad (1.6)$$

For propagating, non-decaying light, all the components of the  $k$ -vector are real and, consequently, less than  $k_0$ . Evanescent waves decay outside the near-field and have an imaginary momentum component in the direction of propagation. This allows perpendicular momentum components directions to be larger than the total momentum vector.

$$\mathbf{k}_{\text{evanescent}} = k_T \hat{\mathbf{T}} + ik_z \hat{\mathbf{L}} \quad (1.7)$$

$$k_0 = \sqrt{k_T^2 - k_z^2} \quad (1.8)$$

$$k_T > k_0 \quad (1.9)$$

where  $\hat{\mathbf{T}}$  and  $\hat{\mathbf{L}}$  point in the transverse and longitudinal directions, respectively.

## 1.5 Imaging

The wavelength of light is what probes feature sizes during interactions and only scatters from features with transverse dimensions  $\geq \lambda/(2n)$ . This value is the diffraction limit. The transverse resolution can be bounded by the longitudinal wavelength because it is a measure of the oscillations of the electric and magnetic fields in the transverse directions.

When light interacts with an object part of it is absorbed, and part of it is scattered. The scattered light can be used to form an image of the object at some distance away from it. Humans see exclusively through scattered electromagnetic radiation. Since light does not scatter off of features with sizes less than  $\lambda/(2n)$ , the images formed from scattered light have no resolution less than the diffraction limit. Ways to image features with these sizes include using a lens or UV incident radiation. Imaging with a lens forms smaller features because the lens material increases the refractive index  $n$  and lowers the diffraction limit. Using UV radiation instead of the visible light detectable by the human eye decreases the probing wavelength. These methods, however, merely alter the value of the diffraction limit, they do not overcome it.

Evanescent waves can have momentum components with magnitudes larger than  $2k_0$  (the momentum representation of the diffraction limit) enabling them to scatter from feature sizes below the diffraction limit. The decay that leads to their large magnitude momentum components, however, prevents them from being detected outside of the near

field ( $\sim 20$  nm). There are near field imaging techniques that take advantage of the evanescent wave probing resolution, but it is not possible to incorporate them into traditional optical microscopes that function in the far-field.

## 1.6 Surface Plasmons

A negative permittivity material is one in which the electric displacement field vector is out of phase with the incident electric field by more than  $90^\circ$ . When an electric field interacts with a material a field is set up in the material due to the bound and free charges with the linear relationship

$$\mathbf{D} = \epsilon \mathbf{E} \quad (1.10)$$

where  $\mathbf{D}$  is the electric displacement field. The permittivity is a measure of the phase between  $\mathbf{E}$  and  $\mathbf{D}$  as

$$\epsilon = \epsilon' + i\epsilon'' = \frac{D}{E} [\text{Cos}(\delta) + i\text{Sin}(\delta)] \quad (1.11)$$

where  $\delta$  is the phase and the imaginary component of the permittivity accounts for absorption. For  $\epsilon' < 0$   $\mathbf{D}$  and  $\mathbf{E}$  point in opposing directions. In the special case of  $\delta = 180^\circ$  where  $\mathbf{D}$  and  $\mathbf{E}$  point in opposite directions,  $\epsilon' = -1$  and  $\epsilon'' = 0$ , and there is no attenuation of the electric displacement field.

A surface plasmon is a collective oscillation of the free electrons at the surface of a material with negative permittivity interfaced with a dielectric. The charge separation sets up an electromagnetic field in a localized region. The surface plasmon oscillates along the surface of the material at the interface and decays in the positive  $z$ -direction. Like the

evanescent wave, it is a nonradiating oscillation with momentum values that are either larger than  $k_0$  or imaginary. The condition for a surface plasmon polariton at a single interface between a negative permittivity metal and a dielectric is as follows:

$$k_{sp} = \frac{\omega}{c} \sqrt{\frac{\epsilon_1 \epsilon_2'}{\epsilon_1 + \epsilon_2'}} \left( 1 + i \frac{\epsilon_2''}{2(\epsilon_2')^2} \right) \quad (1.12)$$

where  $\epsilon_1$  is the permittivity in the incident dielectric,  $\epsilon_2'$  is the real part of the permittivity in the transmitted material and  $\epsilon_2''$  is the imaginary part.

Because surface plasmons are oscillations, they can be excited at their resonant frequency by an external oscillation such as light. In order for the excitation to take place, there must be conservation of energy ( $\omega$ ) and momentum ( $k$ ) in the interaction between the two oscillations. The surface plasmon has momentum components that fall outside the light cone, but these values can match those of an evanescent wave. Fig.1.7 shows graphically the relationship between light and a surface plasmon. It graphs the dispersion curves of  $k$  vs.  $\omega$  for a wave propagating in free space and a surface plasmon polariton at the interface between vacuum and an infinitely thick film of Ag. Everything below the free space dispersion curve is propagating light while everything that falls outside this range has a momentum component that prevents it from radiating and is in the evanescent regime. The surface plasmon dispersion does not couple to propagating light but has energy and momentum values matching those of evanescent waves.

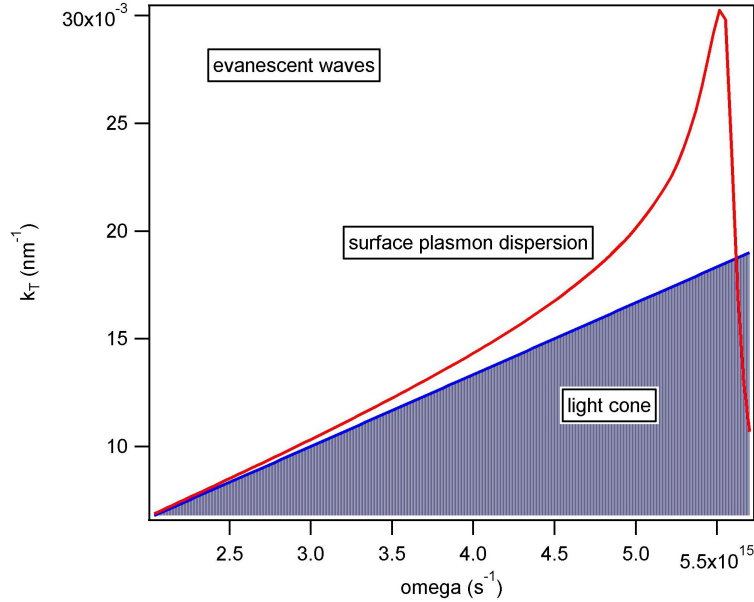


Figure 1.7: Graph of the dispersion curves  $k$  vs.  $\omega$  for the light cone and a surface plasmon at the interface between air and an infinitely thick Ag film.

## 1.7 Coupling

### 1.7.1 Evanescent Wave Productions

In order to excite a surface plasmon with an evanescent wave, one must produce an evanescent wave. Methods include scattering off an object with subwavelength dimensions, total internal reflection, and scattering through a plasmonic grating (this is scattering off an object with subwavelength periodic feature variation). The first method is most directly related to imaging; light scatters off of an object and produces constituent waves with momentum values equivalent to the fourier transform of the dimension sizes. If the dimension is less than the wavelength of light, the fourier transform will have a momentum number greater than  $k_0$  and will fall outside the light cone.

The second method is total internal reflection. When light passes through a high

refractive index material to a low index material, some of it is reflected back. As the incident angle is increased to some system-dependent critical angle ( $\theta_c = \text{Sin}^{-1}(n_2/n_1)$ ) all of the light is reflected and an evanescent wave is set up along the interface to preserve phase conservation through the reflection.

The third method I will discuss is momentum exchange with a plasmonic diffraction grating. The fourier transform of its periodicity is  $2\pi/\Lambda$ , where  $\Lambda$  is the periodicity. Thus, the momentum is inversely proportional to the grating periodicity.

Once an evanescent wave has been generated it must couple to the surface plasmon at its resonance position to gain an enhanced oscillation. For a single interface, the resonance is described by Eq.1.12.

## 1.7.2 Plasmonic Grating Coupling

A plasmonic diffraction grating is a grating with a periodicity smaller than the diffraction limit that can shift the momentum of light between the propagating and evanescent regions. It scatters light through its various diffraction orders, each with a different range of momentum values. An incoming wave with k-vector =  $k_0$  will emerge from the diffraction grating with

$$k_{final} = k_0 + m \frac{2n\pi}{\Lambda} \quad (1.13)$$

where  $m$  is the diffraction order and takes the values  $0, \pm 1, \pm 2, . . .$ . For light scattered through the 0 order, there is no momentum exchange and light emerges with an unaltered k-vector. For the higher orders, there is either a gain or a loss of momentum, depending on the sign of the order. The  $\pm m$  orders are scattered at the same angle on opposite sides

of the normal denoted by Eq.1.8 and are illustrated in Fig.1.8.

$$m\lambda = n\Lambda (\text{Sin}(\theta_m) - \text{Sin}(\theta_i)) \quad (1.14)$$

where  $\theta_m$  is the scattering angle of the diffraction order and  $\theta_i$  is the incident angle. This is converted to momentum space by taking  $k_x = n 2 \pi \text{Sin}(\theta) / \lambda$ . Both the scattering angle of the diffraction orders and the momentum added to the system vary inversely with the periodicity. When the incident light is propagating, the addition of momentum can make it evanescent. Conversely, with incident light that is evanescent, a loss of momentum can shift it to the propagating region. The grating can be tuned to couple incident light to a surface plasmon after a momentum modification by varying the periodicity.

## 1.8 Metamaterials

A metamaterial is an effective medium with dimensions much smaller than the wavelength of incident light. Its optical properties are determined by its geometries and are different from the bulk properties of its constituent materials. One type of metamaterial is the metallo-dielectric multilayer that consists of alternating layers of metal and dielectric films with subwavelength thicknesses. Because the film thicknesses are much smaller than the wavelength, the light does not detect the sharp changes in permittivity and, instead, encounters an effective medium composed of the thickness-weighted average of the two constituent optical properties. In this configuration, the permittivity tensor varies with the thickness ratio of dielectric to metal. The tangential and longitudinal permittivities

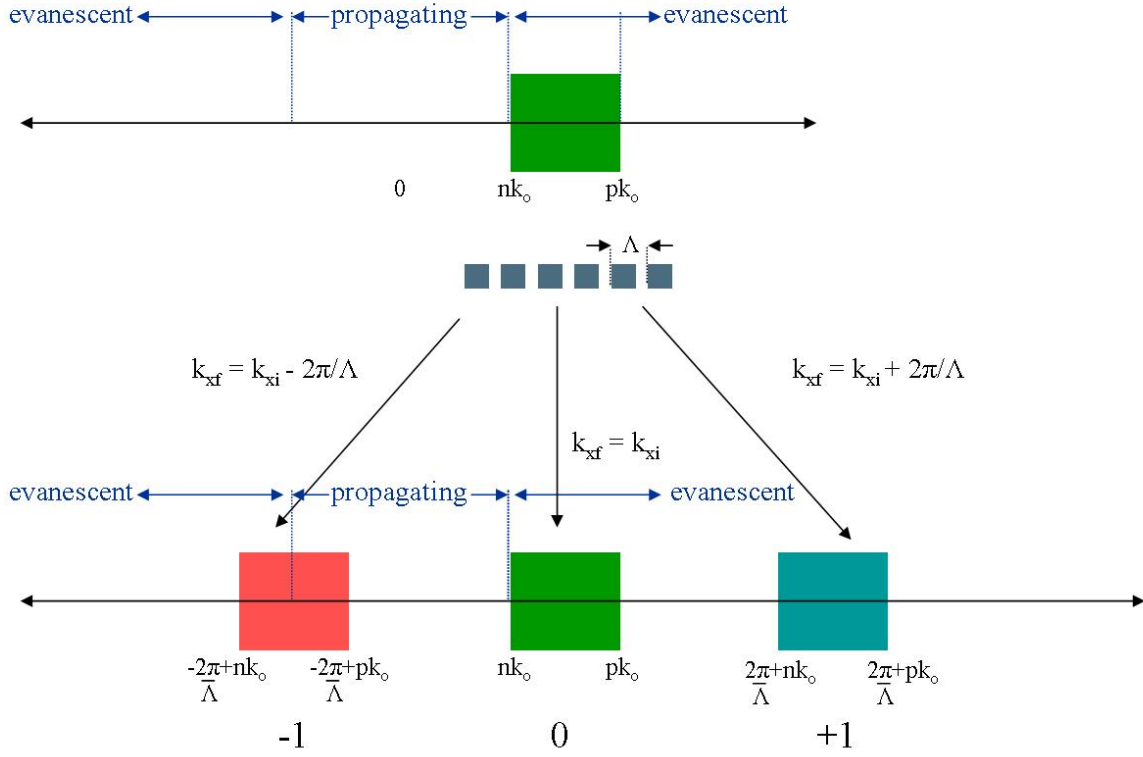


Figure 1.8: Graphical depiction of the momentum exchange that occurs when light scatters through a subwavelength diffraction grating in the 0,  $\pm 1$  diffraction orders.

vary in the following manner:

$$\epsilon_T = \frac{(\epsilon_M + \eta * \epsilon_D)}{(1 + \eta)} \quad (1.15)$$

and

$$\frac{1}{\epsilon_L} = \left( \frac{1}{\epsilon_M} + \frac{\eta}{\epsilon_D} \right) (1 + \eta) \quad (1.16)$$

where  $\epsilon_M$  and  $\epsilon_D$  are the permittivities of the metal and dielectric, respectively, and  $\eta$  is the thickness ratio.

Fig.1.9 shows the behavior of the components of the permittivity tensor as the dielectric-metal thickness ratio,  $\eta$ , is varied from 0 to 5 for a Ag-Al<sub>2</sub>O<sub>3</sub> metamaterial. The transverse component (on the left) of the permittivity tensor increases smoothly from  $\eta=0$  where it

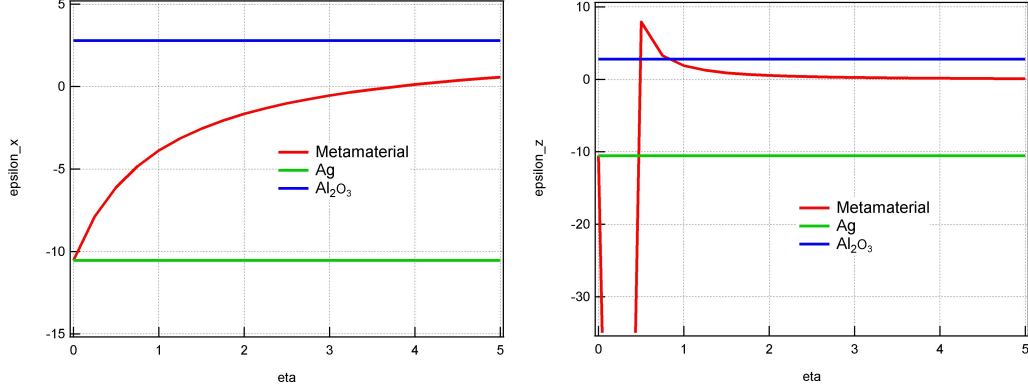


Figure 1.9: The transverse (left) and longitudinal (right) components of the permittivity tensor of a Ag-Al<sub>2</sub>O<sub>3</sub> multilayer metamaterial, Ag, and Al<sub>2</sub>O<sub>3</sub> as a function of  $\eta$ , the dielectric to metal thickness ratio.

is the metal permittivity, along a curve that approaches the permittivity of the dielectric separating the metal layers. The longitudinal component (on the right) matches the metal permittivity at  $\eta=0$ , then drops to  $\sim 15$  times the metal value by  $\eta=0.25$ , climbs to  $\sim 3x$  the dielectric permittivity at  $\eta=0.6$ , then drops just below the dielectric permittivity level by  $\eta = 0.75$ , and remains relatively constant over a large range of  $\eta$ . The metamaterial can only support surface plasmons where there is a negative component to the permittivity tensor, which means for the Ag-Al<sub>2</sub>O<sub>3</sub> metamaterial used to calculate Fig.1.9 that  $\eta$  must be between 0 and 3.5 for the transverse component to be negative and between 0 and 0.5 for the longitudinal component to be negative. For a medium with an anisotropic permittivity tensor, the decomposition of the momentum vector is as follows:

$$k_0^2 = \frac{k_T^2}{\epsilon_L} + \frac{k_L^2}{\epsilon_T} \quad (1.17)$$

Where  $k_0$  is the total momentum,  $k_T$  is the transverse momentum component, and  $k_L$  is the longitudinal momentum component. When one of the permittivities is negative, the

perpendicular momentum component can be larger than the light cone.

In Fig.1.9 the materials selected are Ag and  $\text{Al}_2\text{O}_3$ . Ag possesses a negative permittivity that can support surface plasmons and has the smallest absorption of common metals in the visible. Since surface plasmons are an inherently lossy oscillation, Ag was also chosen to minimize decay losses. The dielectric chosen for the example was  $\text{Al}_2\text{O}_3$ , a transparent oxide with low absorption than can be grown in a uniform film. The meta-

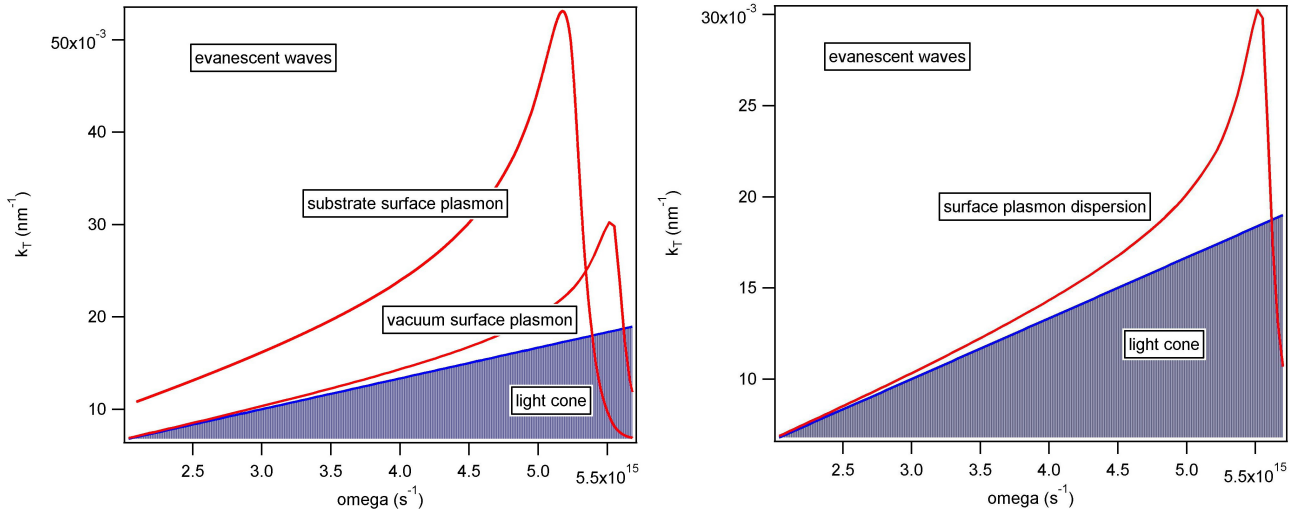


Figure 1.10: Left: The dispersion relations of a thin Ag film on a glass substrate in vacuum for the free space light cone and the surface plasmons generated at the vacuum-Ag and Ag-glass interfaces. Right: The dispersion relations of an infinitely thick Ag film in vacuum for the free space light cone and the surface plasmon generated at the interface.

material permittivity can be tuned because unlike a thin film of negative permittivity metal which supports surface plasmons at only two interfaces, the metamaterial has surface plasmons at each interface. These plasmons interfere with one another, shifting the resonant momentum value and increasing the number of supported modes. Fig.1.10 shows the dispersion of supported plasmon modes for an infinitely thick Ag film with only the Ag-vacuum interface and a thin Ag film on a glass substrate that supports plasmon modes at the vacuum-Ag interface and the Ag-glass interface.

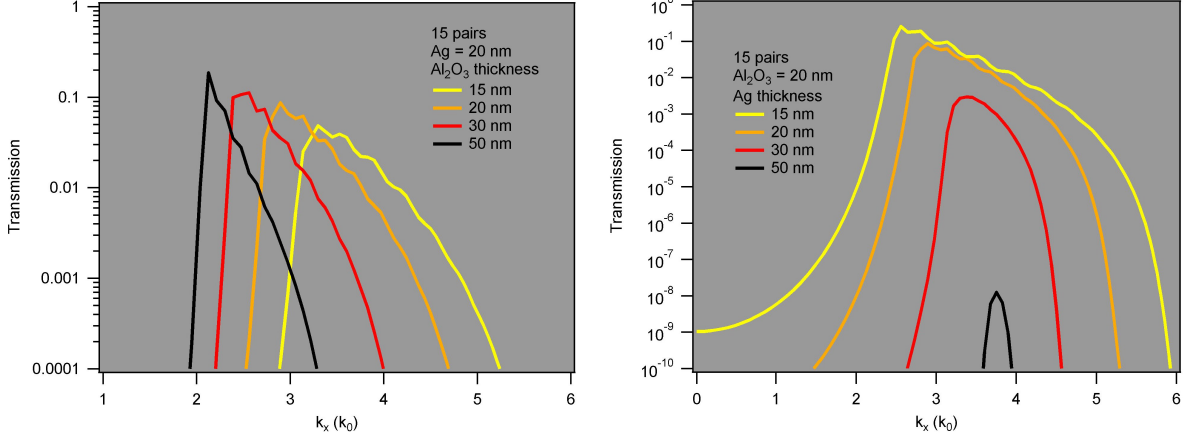


Figure 1.11: The simulated transmission of TM polarized 532 nm light vs. transverse momentum for a 15 pair Ag-Al<sub>2</sub>O<sub>3</sub> metamaterial. Left: The Ag thickness is 20 nm and the Al<sub>2</sub>O<sub>3</sub> is varied from 15 nm to 50 nm. Right: the Al<sub>2</sub>O<sub>3</sub> is a constant 20 nm and the Ag is varied from 15 nm to 50 nm.

The change in thickness ratio alters the permittivity tensor, which controls the resonant momentum and frequency of the surface plasmons (see Eq.1.12). Fig.1.11 illuminates the shift of surface plasmon momentum with varying film thicknesses. It shows the simulated transmission of a 15 pair Ag-Al<sub>2</sub>O<sub>3</sub> metamaterial in an n=6 medium under 532 nm TM illumination as a function of tangential momentum. In the high refractive index medium, there is coupling between surface plasmons and the light cone up to  $6(2\pi/\lambda)$  and the transmission in the far-field is nonzero. On the right, the Ag film thickness is held constant at 20 nm and the oxide thickness is varied from 15 nm to 50 nm ( $\eta = 0.75$  to 2.50). On the left, the Al<sub>2</sub>O<sub>3</sub> thickness is held constant and the Ag film thickness is varied with  $\eta = 1.33$  to 0.40. The incident tangential momentum change was achieved by varying the incidence angle from 0.01 ° to 89.99 ° as

$$k_T = n * \frac{2\pi}{\lambda} \text{Sin}(\theta) \quad (1.18)$$

where  $\theta$  is the incident angle,  $\lambda$  is the incident wavelength, and  $n$  is the refractive index. The transmission peak in the artificially high refractive index material is an indirect measure of the surface plasmon momentum: momentum values at which a peak in transmission occurs denote that the excitation of surface plasmon polariton by a propagating incident wave. Examination of the simulated transmission reveals that decreasing the  $\text{Al}_2\text{O}_3$  thickness shifts the resonance to higher momentum values and broadens the resonance peak. A thinner oxide for imaging will result in high subdiffraction-limited resolution and a wider range of feature sizes that can be detected. Decreasing the Ag film from 50 nm to 15 nm also shifts the resonance to higher momentum values. Importantly, the thicker Ag is more absorbing and the change from 15 to 50 nm decreases the transmission by 7 orders of magnitude. It is preferable to have the thinnest possible Ag and change the  $\text{Al}_2\text{O}_3$  layer to minimize absorption losses.

The software used to simulate these transmission curves as well as those in later chapters for metamaterials with plasmonic gratings was written in Mathematica by my group. It is based on the methodology of Tikhodeev (Tikhodeev et al., 2002). This matrix method begins with the assumption that the space of interest is periodic in its optical properties along a tangential direction.

$$\epsilon(r) = \epsilon(r + R) \tag{1.19}$$

where  $r$  is the position,  $R$  is the characteristic length of the system or periodicity, and  $\epsilon$  is the permittivity. The system is built up by stacking slabs of periodic material on top of one another and specifying the materials in a slab, the periodicity in the  $x$ - and  $y$ -directions, and the slab thickness. When performing the simulation, the program defines

the electric field in the following manner:

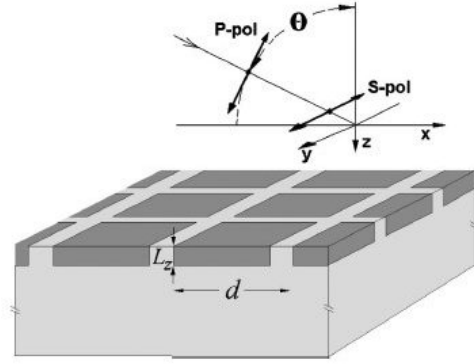


Figure 1.12: Schematic structure of a square-patterned layer on a substrate. Light grey: material 1; dark grey: material 2. The coordinate origin  $z=0$  is at the surface of the structure.

$$E(x, y, z, t) = E_G \exp[ik_{x,G}x + ik_{y,G}y + \exp[iKz - i\omega t]] \quad (1.20)$$

with

$$k_{x,G} = \frac{2\pi}{\lambda} \text{Sin}(\theta) \text{Cos}(\phi) + \frac{2\pi}{\Lambda_x} g_x \quad (1.21)$$

$$k_{y,G} = \frac{2\pi}{\lambda} \text{Sin}(\theta) \text{Sin}(\phi) + \frac{2\pi}{\Lambda_y} g_y \quad (1.22)$$

where  $g_{\pm} = 0, \pm 1, \pm 2, \dots$  denotes the harmonic number, and  $\theta$  and  $\phi$  are the zenith and azimuthal angles. Then, it solves the eigenvector equation of one slab for the electric field with

$$Z e_{x,y} = K^2 e_{x,y} \quad (1.23)$$

It builds these eigenvalues at each of the slabs through the whole stack until the final interface is reached to solve for transmission, reflection, absorption, electric field, and magnetic field. For physically real results, the materials used must be isotropic in x and

y and nonmagnetic with smooth boundaries.

Surface plasmons in a negative permittivity material that are excited at their frequency resonance can enhance the incident signal. Light can couple to surface plasmons but must match their momentum and frequency values. Propagating light inside the light cone has smaller momentum components than do the surface plasmons and cannot couple to them. Evanescent waves, however, have larger momentum components at a given frequency and can couple to surface plasmons at their resonant frequency, resulting in an enhanced signal. One way to generate evanescent waves is interaction with a photonic grating with periodicity smaller than the wavelength of the incident light. The momentum exchanged between the light and the grating is inversely proportional to the periodicity. In the higher positive diffraction orders, propagating light can gain momentum and be shifted to the evanescent regime. Additionally, metamaterials play a crucial role in the light-matter interaction through their adjustable dispersion relationship. The dispersion relation of the surface plasmons in a metamaterial varies with the ratio of the dielectric and metal thickness and can be tuned such that the momentum coupling value between evanescent waves and surface plasmons is maximized in a desired wavelength range.

## CHAPTER 2

### CREATION AND DETECTION OF ENHANCED EVANESCENT WAVES IN THE FAR-FIELD

#### **Abstract:**

I demonstrate the fabrication of a simple metamaterial - diffraction grating device that both amplifies and converts evanescent waves into propagating ones. This is the most accessible example of such phenomena reported until now as it requires few thin film layers, operates in the visible, and can be probed with traditional optics. The metamaterial exhibits amplification of evanescent waves generated from total internal reflection. The device was fabricated over  $1 \text{ cm}^2$  using pulsed laser deposition and a pattern replication technique.

A fast method to acquire optical images with resolution beyond the diffraction limit is a long standing scientific challenge. Current serial methods like near field scanning microscopy form an image pixel by pixel, which is subwavelength resolved but very time consuming to create. Standard optical microscopy is real time but loses the evanescent

waves that carry high spatial frequency information since they do not propagate in free space (Abbe, 1873). Recently, Pendry showed that a material with both negative permittivity and permeability amplifies evanescent waves and allows them to propagate through it (Pendry, 2000). While these materials do not exist in nature, metal-dielectric metamaterials with anisotropic permittivities also perform a similar task for TM polarized light via coupling to surface plasmons (Smith and Schurig, 2003; Kuhta et al., 2007; Salandrino and Engheta, 2006; Tomita et al., 2008; Cai et al., 2005; Economou, 1969).

Since the evanescent waves do not propagate past the metamaterial, only a near-field image is formed at the far surface of the metallo-dielectric structure. The upper limit on thickness to allow transmission is limited by the intrinsic metallic losses. Several solutions have been proposed to form magnified far-field images. A cylindrical hyperlens has been shown to resolve an incident two source wave as a function of the ratio of radii of curvature (Liu, 2007; Jacob et al., 2006). Another method is based on combining oblique superlenses of metallo-dielectric films to spread the image by altering the path lengths of each scattered ray (Salandrino and Engheta, 2006; Zhao et al., 2008). More recently, diffraction gratings have been proposed to convert the amplified evanescent waves into propagating ones creating a far-field superlens (FSL) (Liu et al., 2007; Zhang et al., 2007; Fang et al., 2005; Durant et al., 2006; Xiong et al., 2007b; Xiong et al., 2007a). In this approach, the negative diffraction orders of the grating convert the longer evanescent  $k$ -vectors into propagating ones as described by the simple diffraction condition  $k_{final} = k_x \pm m \cdot 2\pi/\Lambda$  where  $m$  is the diffraction order,  $\Lambda$  is the diffraction grating periodicity, and  $k_x$  and  $k_{final}$  are the grating incident and scattered transverse  $k$ -vectors, respectively.

Currently, state of the art demonstrations of these processes require the use of E-beam lithography tools and have been experimentally demonstrated only outside the visible range.

In this chapter I present an accessible fabrication and characterization method to demonstrate the amplification and conversion of evanescent waves into propagating ones. I create a functional structure that amplifies ( $k_x = 1.2 \cdot k_o$ ) waves and allows for their collection with a far-field detector. This is the first experimental verification in the visible for tuned metamaterials made by such processes necessary for far-field subwavelength imaging. My technique has the benefits of rapid fabrication with minimal resources, quick data acquisition time, and scalability over large areas. I designed the metamaterial structure using a fast algorithm based on the scattering-matrix formalism that calculates the optical transmission properties in a periodic photonic crystal slab of finite thickness. Maxwell's equations are solved as an eigenvalue problem via plane-wave decomposition in two-dimensional Cartesian coordinates, and the solution is propagated across the different layers by means of scattering matrices, which define the continuity conditions for electromagnetic field components at each interface (Tikhodeev et al., 2002). I use this model to determine the adequate number of layers and thicknesses for amplification of the evanescent waves available from total internal reflection of a glass-air interface.

## 2.1 The Ideal Superlens

The perfect superlens functions by coupling to and transmitting both propagating and evanescent waves and has a refractive index  $=-1$  where both the permittivity and

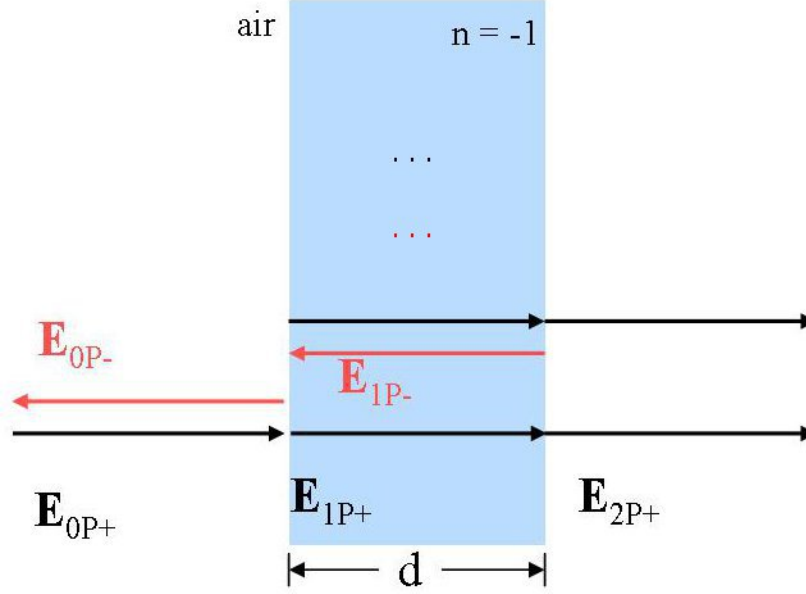


Figure 2.1: A diagram of the transmissions and reflections of the electric field that occur for a TM polarized wave at each interface of vacuum and an  $n = \sqrt{\epsilon\mu} = \sqrt{-1 \cdot -1} = -1$  film of thickness  $d$ .

permeability are equal to -1. The propagating waves meet the interface and are refracted according to Snell's law ( $n_1 \sin[\theta_1] = n_2 \sin[\theta_2]$ ) to a focus inside the lens. They spread, and then at the second interface, focus again at a position equidistant from the transmitted side of the lens to the original distance from the incident side of the lens.

Also, the object must be in the near field of the lens in order for evanescent waves to reach the surface, but once they do, they couple to surface plasmons and are enhanced in the superlens. When they emerge from the transmitted side, the enhanced evanescent waves begin to decay and reform with the propagating waves to create a perfect image of the scattering object with ultra-high resolution in the near field of the transmitted side of the superlens. The evanescent wave enhancement can be derived mathematically through examination of the transmission in the system. First, note that  $n = \sqrt{\epsilon\mu}$  and that  $\epsilon = \mu = -1$ . Then, the electric field of a p-polarized wave traveling in the positive  $z$  direction is

described as

$$\mathbf{E}_{0P+} = [1, 0, 0]exp(ik_z z + ik_x x - i\omega t) \quad (2.1)$$

with

$$k_z = +i\sqrt{k_x^2 + k_y^2 - \omega^2 c^{-2}} \quad (2.2)$$

and

$$\omega^2 c^{-2} < k_x^2 + k_y^2 \quad (2.3)$$

The electric field transmitted into the superlens becomes

$$\mathbf{E}_{1P+} = t[1, 0, 0]exp(ik'_z z + ik_x x - i\omega t) \quad (2.4)$$

with

$$k'_z = +i\sqrt{k_x^2 + k_y^2 + \epsilon\mu\omega^2 c^{-2}} \quad (2.5)$$

and

$$\epsilon\mu\omega^2 c^{-2} < k_x^2 + k_y^2 \quad (2.6)$$

The transmission and reflection coefficients are given by

$$t = \frac{2\epsilon k_z}{\epsilon k_z + k'_z} \quad (2.7)$$

$$t' = \frac{2k_z}{\epsilon k_z + k'_z} \quad (2.8)$$

$$r = \frac{\epsilon k_z - k'_z}{k'_z + \epsilon k_z} \quad (2.9)$$

$$r' = \frac{k'_z - \epsilon k_z}{k'_z + \epsilon k_z} \quad (2.10)$$

The transmittance is then

$$T_P = tt' \exp(ik'_z d) + tt' r'^2 \exp(3ik'_z d) + tt' r'^4 \exp(5ik'_z d) + \dots \quad (2.11)$$

This is a geometric series that converges to

$$T_P = \frac{tt' \exp(ik'_z d)}{1 - r'^2 \exp(2ik'_z d)} \quad (2.12)$$

Taking the limit where  $\epsilon$  and  $\mu$  go to -1 for a perfect superlens

$$\lim_{\epsilon \rightarrow -1, \mu \rightarrow -1} T_P = \lim_{\epsilon \rightarrow -1, \mu \rightarrow -1} \frac{2\epsilon k_x}{\epsilon k_z + k'_z} \frac{2k'_x}{\epsilon k_z + k'_z} \frac{\exp(ik_z d)}{1 - \exp(2ik'_z d) (k'_z - \epsilon k_z)^2 / (k'_z + \epsilon k_z)^2} \quad (2.13)$$

$$= \exp(-ik'_z d) = \exp(-k_z d) \quad (2.14)$$

This is a nonzero number that indicates the transmission of evanescent waves through a superlens of thickness  $d$ . Such transmission does, however, require a material with both negative permittivity and negative permeability. Such materials do not exist in nature, but materials with only negative permittivity do. The negative permittivity material can be utilized for TM polarized waves in the quasistatic limit where the wavelength of light is much much larger than the dimensions of the superlens ( $\omega \ll c\sqrt{k_x^2 + k_y^2}$ ). This regime

alters  $k_z$  and decouples the dependence on  $\mu$  and  $\epsilon$  at the loss of polarization independence.

$$\lim_{k_x^2+k_y^2 \rightarrow \infty} k_z = \lim_{k_x^2+k_y^2 \rightarrow \infty} i\sqrt{k_x^2+k_y^2-\omega^2c^{-2}} \quad (2.15)$$

$$= i\sqrt{k_x^2+k_y^2} \quad (2.16)$$

$$\lim_{k_x^2+k_y^2 \rightarrow \infty} k'_z = \lim_{k_x^2+k_y^2 \rightarrow \infty} i\sqrt{k_x^2+k_y^2-\epsilon\mu\omega^2c^{-2}} \quad (2.17)$$

$$= i\sqrt{k_x^2+k_y^2} = k_z \quad (2.18)$$

which yields for the transmittance after calculating the transmission coefficients,

$$\lim_{k_x^2+k_y^2 \rightarrow \infty} T_P = \lim_{\epsilon \rightarrow 1, \mu \rightarrow 1} \frac{2\epsilon k_x}{\epsilon k_z + k'_z} \frac{2k'_x}{\epsilon k_z + k'_z} \frac{\exp(ik_z d)}{1 - \exp(2ik'_z d)(k'_z - \epsilon k_z)^2 / (k'_z + \epsilon k_z)^2} \quad (2.19)$$

$$= \frac{4\epsilon \exp(ik'_z d)}{((\epsilon + 1)^2 - \epsilon - 1)^2 \exp(2ik_z d)} \quad (2.20)$$

$$\lim_{k_x^2+k_y^2 \rightarrow \infty, \epsilon \rightarrow -1} T_P = \lim_{\epsilon \rightarrow -1} \frac{4\epsilon \exp(ik'_z d)}{((\epsilon + 1)^2 - \epsilon - 1)^2 \exp(2ik_z d)} \quad (2.21)$$

$$= \exp(-ik_z d) = \exp(+d\sqrt{k_x^2+k_y^2}) \quad (2.22)$$

## 2.2 Fabrication

The device was fabricated by depositing five pairs of alternating layers of 20 nm Ag and 100 nm Al<sub>2</sub>O<sub>3</sub> via pulsed laser deposition with a KrF excimer laser operating at a wavelength of 248 nm, pulse energy of 300 mJ (pulse fluence  $\sim 1$  mJ/cm<sup>2</sup>), and at 40 Hz onto a glass substrate. The diffraction grating with periodicity in the  $x$ -direction was

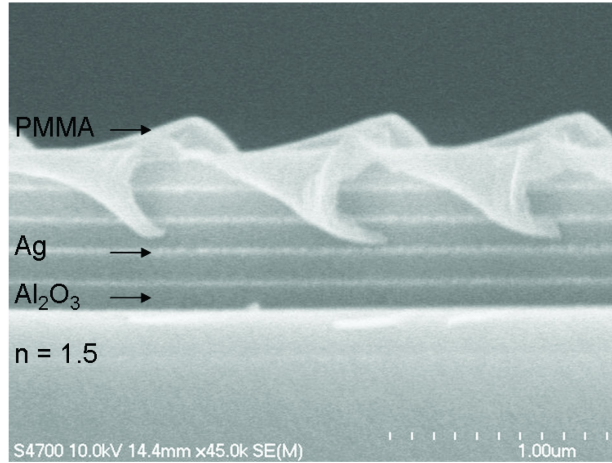


Figure 2.2: Electron micrograph of the metallodielectric and grating structure. Visible are 10 alternating layers of 20 nm Ag and 100 nm  $\text{Al}_2\text{O}_3$  on a glass substrate. The PMMA blaze diffraction grating has an 830 nm periodicity and 196 nm height. The large overhang is PMMA resulting from preparing the sample for cross section imaging.

stamped out of a 4% polymethyl methacrylate (PMMA) solution over an entire  $1 \text{ cm}^2$  area. A mold for stamping was made by replicating a blazed diffraction grating: 830 nm periodicity and 196 nm height. Fig. 2.2 shows an electron micrograph of the final structure. The replication process is based on patented PRINT<sup>®</sup> (Pattern Replication In Nonwetting Templates)(Rolland et al., 2005) technology that utilizes perfluoropolyether (PFPE) elastomers as a reusable molding material for soft lithography. PFPE elastomers as a molding material have advantages over their silicone-based counterparts because their very low surface energy, inertness, and tunability permit them to form arrays of sub-100 nm features that can be easily separated from the mold. Application of this technique is important since FSLs capable of amplifying long k-vector evanescent waves will undoubtedly require gratings with pitch sizes in the 100 nm range.

## 2.3 Experiment and Simulation

For the optical experiment, incident evanescent waves are produced with total internal reflection by mounting the device on the back of a half disk glass prism ( $n=1.5$ ) with index matching oil ( $n=1.51$ ) at the eucentric point of a source and detector arm. The 532 nm CW laser source is rotated around the grating to create larger incident  $k_x$  vectors. The optical constants of silver force evanescent waves to originate from the matching oil-metal interface (Kretschmann–Raether configuration). Light incident past the critical angle generates evanescent waves ( $k_x \geq k_o$ ) that can not propagate in free space. Proper alignment to ensure in-plane scattering is achieved with rotational mounts in the  $x$ - $z$  and  $x$ - $y$  planes. Transmitted light is collected with an amplified Si photodiode and connected to a data collection system where it is normalized to a reference beam. Fig. 2.3 shows a schematic of the set-up.

Figs. 2.5 and 2.6 are the experimental transmission measurements along with simulations of the -1 and 0 diffraction orders through the structure from the TM and TE polarizations.

The TM -1 diffraction order has a low intensity for propagating waves ( $k_x \leq k_o$ ) but a large transmission peak centered at  $k_x = 1.2 \cdot k_o$ , indicating the amplification of evanescent waves ( $k_x > k_o$ ) and their conversion into free space propagating ones.

The fact that the metamaterial can enhance evanescent waves is explained by the dispersion relationship of the metal-dielectric multilayers (See Fig.2.4). Evanescent waves with momentum values between the free space light line and glass light line at a given

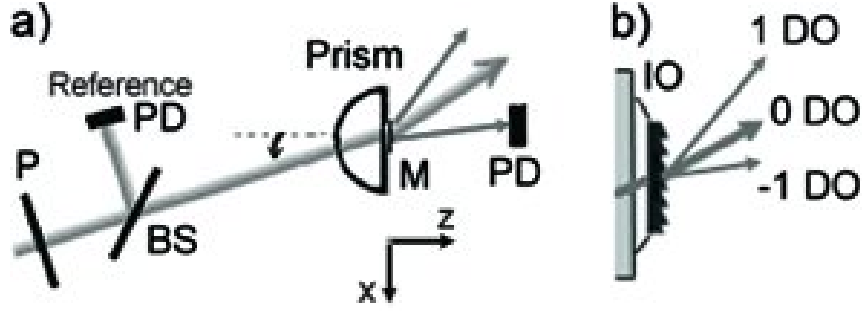


Figure 2.3: a) Schematic setup to realize amplification and collection of evanescent waves with visible range optics. The incident and collection arms can be rotated to vary the incident  $k_x$  value and capture all three diffraction orders. b) Detail of the metamaterial and grating. In the diagrams P stands for the polarizer, BS is the beamsplitter, PD is photodiode detector, M is the metamaterial, DO is the diffraction order and IO is index-matching oil.

frequency can couple to surface plasmons supported in the metamaterial. For TM polarization, this relationship is presented in Eq. 2.23:

$$\frac{k_x^2}{\epsilon_z} + \frac{k_z^2}{\epsilon_x} = k_o^2 \quad (2.23)$$

where  $\epsilon_x = (\epsilon_{metal} + \eta \cdot \epsilon_{dielectric}) / (1 + \eta)$  is the effective transverse permittivity,  $1/\epsilon_z = (1/\epsilon_{metal} + \eta/\epsilon_{dielectric}) / (1 + \eta)$  is the effective longitudinal permittivity,  $\eta$  is the dielectric to metal ratio,  $k_o$  is the free space wave vector, and  $k_x$  and  $k_z$  are the transverse and longitudinal k-vectors, respectively (Tretyakov, 2000). It can be observed that negative values of  $\epsilon_x$  will allow propagation of incident waves with  $k_x$  larger than the free space propagation vector. This is possible due to the negative permittivity of the metallic layers whose surface plasmons are excited by the incident evanescent waves. Interaction of the plasmons at each metal-dielectric interface causes the modes to split and alters the coupling wavelength, giving metamaterials some transmission bandwidth and tunability instead of

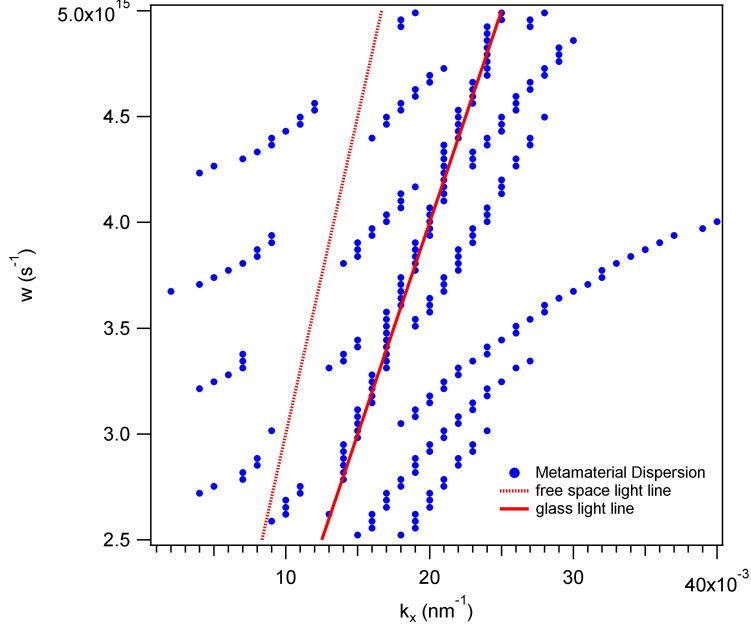


Figure 2.4: Numerical calculation of the dispersion relation of a 5 pair Ag-Al<sub>2</sub>O<sub>3</sub> metamaterial (blue circles), with the free space light cone,  $k_0$  (red dashed line), the substrate light cone, and  $1.5k_0$  (solid red line). The modal wave number at 532 nm is  $0.0142 \text{ nm}^{-1}$ .

one discrete coupling wavelength as occurs in single metal-dielectric interfaces (Cai et al., 2005; Economou, 1969; Wang et al., 2008b; Xiong et al., 2007b). Fig. 2.4 shows where this tuned coupling can be achieved. It depicts the surface plasmon modes supported by the metamaterial, the free space light line, and the  $n=1.5$  light line. Long momentum vectors up to  $n \cdot k_0$  are produced from the high refractive index prism.

On the other hand, the TM 0 order exhibits the transmission cutoff for  $k_x > k_o$  as these evanescent photons do not exchange momentum with the grating. The symmetric +1 diffraction order (not shown) is observed as well, holding a constant intensity until its cutoff at  $k_x = 0.5 \cdot k_o$  following the simulation prediction.

While TE incidence produces evanescent waves as well, this polarization does not couple to the surface plasmons and I expect to see no transmission in the -1 order past  $k_x > k_o$ . This is an important fact since in the absence of the metamaterial layer, both TE

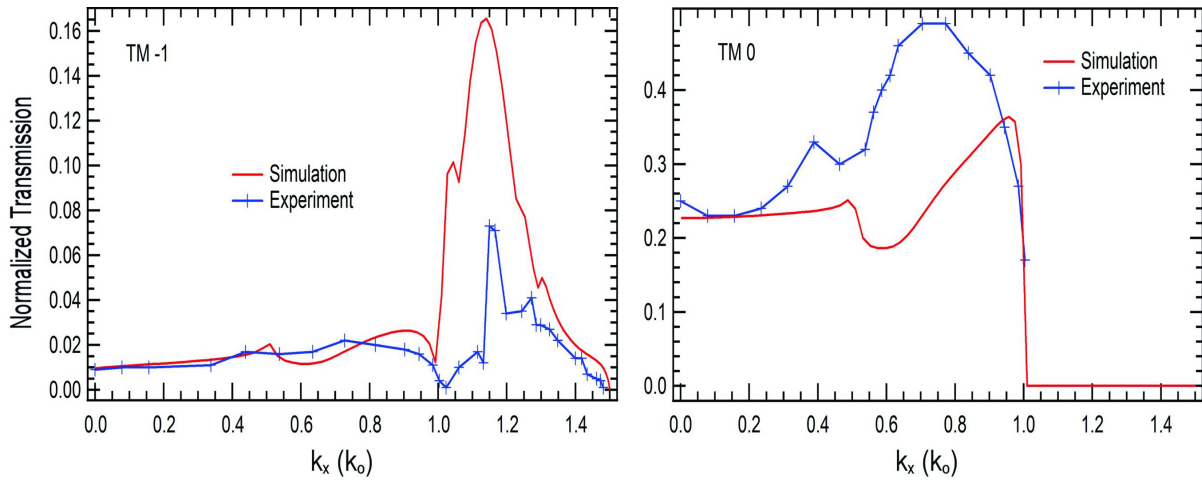


Figure 2.5: Normalized transmission versus relative k-vector for TM incident light. Left, the -1 diffraction order demonstrates conversion of evanescent wavelengths into propagating light. Right, the 0 diffraction order shows no propagation for evanescent waves.

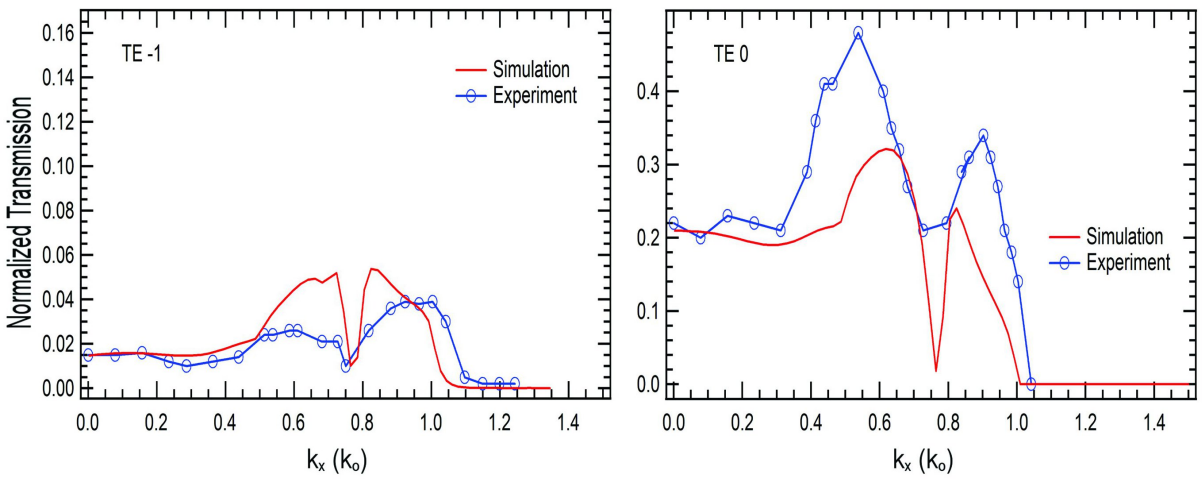


Figure 2.6: Normalized transmission versus relative k-vector for TE incident light. The -1 (right) and 0 (left) diffraction orders exhibit no evanescent propagation.

and TM evanescent waves would be converted to free propagating -1 modes of extremely low intensity by the grating. Fig. 2.6 demonstrates this statement and completes the characterization of the device.

It can be noted that the design simulations (zero fitting parameters) do not lie on top of the experimental data. This fact could be due to the 5 % uncertainty in the actual material parameters of the fabricated layers and the curved surface of the half disk prism that presents slight lensing effects, spreading the beam in the  $x$ -direction. Also, the diffraction grating simulated has a blaze profile that was step-like, rather than a continuous triangle. Experimental results do show homogeneity, however, across the entire 1 cm<sup>2</sup> area of the patterned grating.

## 2.4 Conclusions

In conclusion, I have demonstrated a simple metamaterial-diffraction grating device that both amplifies and converts evanescent waves into propagating ones. This is the most accessible demonstration reported until now since it requires few thin film layers, operates in the visible, and can be probed with traditional optics. The device was fabricated over 1 cm<sup>2</sup> using PRINT<sup>®</sup>, a replication technique that besides providing a large area is also capable of sub-100 nm resolution, a key feature to realizing far-field superlenses capable of high spatial resolution.

## CHAPTER 3

# NUMERICAL DESIGN AND SCATTERING LOSSES OF A 1D METALLO-DIELECTRIC MULTILAYER WITH BROADBAND COUPLING OF PROPAGATING WAVES TO PLASMON MODES IN THE VISIBLE RANGE

### **Abstract:**

I report on the design, fabrication and optical characterization of a 1D metallo-dielectric metamaterial tuned to enhance evanescent wave transmission with  $k_x \leq 4k_0$ . Taking reflection and transmission measurements from a 1D subwavelength diffraction grating placed on the metamaterial, I show broadband propagating wave to surface plasmon coupling in the visible. However, the fabricated device falls short of the design expectations based on coupled-wave numerical simulations. The dips in the reflection spectrum associated with surface plasmon coupling are 40 % smaller than predicted and the transmission exhibits strong depolarization. Overall, the numerical results support that intrinsic metallic losses do not preclude the development of these devices in the visible but there are considerable plasmon scattering losses from the metamaterial's imperfections. This extrinsic limiting factor needs to be overcome to develop metallo-dielectric metamaterials for practical com-

ponents for use in superlenses.

In 2000, Pendry's work demonstrating the enhancement of evanescent waves in a negative refractive media sparked interest in experimental verification of a superlens (Pendry, 2000). In the quasistatic limit, where the dimensions of the lens are much smaller than the wavelength of light, for TM waves, the material needs only to have  $\epsilon < 0$  and the evanescent wave enhancement is mediated by surface plasmon polaritons. Unfortunately, surface plasmons are intrinsically lossy modes and the material's absorption presents a great challenge for practical realizations of evanescent wave amplification. Combining negative permittivity materials with dielectrics at subwavelength scales to form metamaterial structures has been shown theoretically to mitigate evanescent wave losses (Ramakrishna et al., 2003) and allow demonstration of ultra high resolution imaging (Cai et al., 2005; Xiong et al., 2007a; Salandrino and Engheta, 2006; Fang et al., 2005; Xiong et al., 2007b). Metallo-dielectric metamaterials also permit fine tuning of the enhancement to target desired ranges of evanescent waves and/or light frequencies by adjusting the system geometry and the resulting anisotropic permittivity tensor (Wood et al., 2006).

Since the metals commonly used in metamaterials have the lowest absorption losses in the near UV (i.e. Ag absorption coefficient  $\alpha_{360nm} = 0.054 \text{ nm}^{-1}$  and  $\alpha_{630nm} = 0.079 \text{ nm}^{-1}$ ) (Palik, 1985), most optical metamaterials research concentrated on this range (Cai et al., 2005; Wang et al., 2008a; Melville and Blaikie, 2005; Liu et al., 2003; Wang et al., 2008b). Evanescent wave amplification in a broadband visible range remains still highly

desirable and relatively unexplored.

In this chapter, I present a numerical and experimental study of the optical properties of a 1D metamaterial. I show that intrinsic losses are not an insurmountable barrier for broadband visible application of these metamaterials, but extrinsic nanofabrication defects generate significant plasmon scattering losses from the metamaterial's imperfections and thus are the current limiting factor. I tuned the metamaterial to enhance evanescent wave transmission with transverse propagation vectors ( $k_x$ ) four times larger than those in free space and exhibiting broadband evanescent wave to surface plasmon coupling across the visible. The optical properties of the fabricated device have been characterized with simple reflection and transmission measurements from light incident on a subwavelength periodicity grating on top of the metamaterial. They follow the overall trends of the numerical design, but the TE and TM polarized optical transmissions and reflections present less contrast than expected. In particular, the amplitude of the reflection features that signal the plasmon coupling in the TM mode are 40 % smaller than those in the simulations and the spectral transmission also exhibits a strong depolarization component.

The metamaterial that is the subject of this study consists of an  $\text{Al}_2\text{O}_3$ -Ag multilayer. I simulated its transmission and reflection properties using a numerical method based on the transfer/scattering matrix method (Tikhodeev et al., 2002). In order to design the device response to evanescent waves, a propagating wave was launched from an artificially high index material ( $n = 4$ ), since the continuity of Maxwell's equations across boundaries require the  $k_x$  components to be equal in coupling evanescent waves from vacuum or propagating waves from the high index media (Xiong et al., 2007b). Thus, the incident

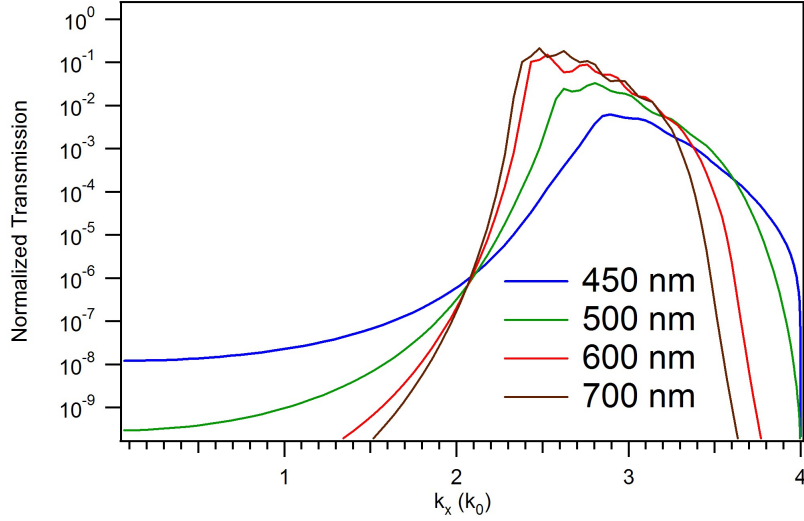


Figure 3.1: TM Transmission coefficients vs.  $k_x$  of the metamaterial in an  $n = 4$  medium at wavelengths  $\lambda = 450, 500, 600, 700$  nm.

waves have a propagation vector analogous to that of an evanescent wave for  $k_x > k_o$  and regular propagating response at lower incidence angles  $k_x < k_o$ .

### 3.1 Simulation and Fabrication

The numerical tools were used to optimize the device parameters (number of layers and thicknesses) to maximize contrast between transmitted propagating waves and amplified evanescent waves. The final design consists of a 10 pair  $\text{Al}_2\text{O}_3$ -Ag metamaterial. The thicknesses are 29.5 nm and 27 nm, respectively. Fig. 3.1 presents the modeled performance for the metamaterial embedded in the design medium. Significant transmission of  $k_x > 2.5k_o$  all across the visible range can be observed. Contrast of more than 10 and 5 orders of magnitude, respectively, between the transmission of TM vs. TE waves and between the evanescent and propagating windows is achieved simultaneously (not shown).

The dispersion relationship of the resulting metamaterial in vacuum was calculated

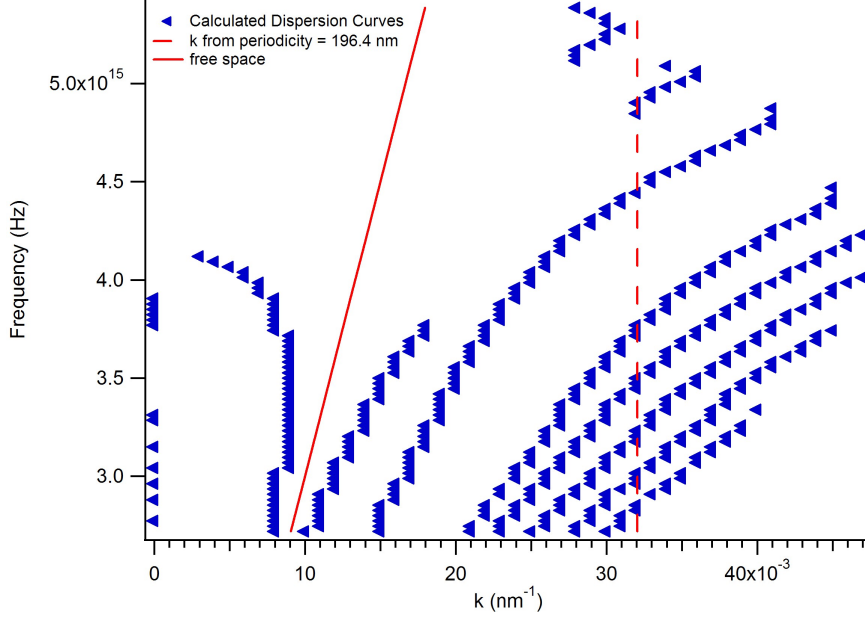


Figure 3.2: Dispersion relation for a 10 pair  $\text{Al}_2\text{O}_3$  and Ag metamaterial with layer thickness 29.5 and 27 nm, respectively. The solid red line is the free space light line, the dashed line is the  $k_x$ -vector created by the 196.4 nm periodicity diffraction grating, and the blue triangles are the dispersion curves.

using the matrix formalism developed by Davis (Davis, 2009) (Fig. 3.2). It shows the existence of multiple surface plasmon polariton branches that cross the visible range frequencies, supporting the possibility of broadband coupling. Placing a grating at the top of the structure allows the launching of evanescent waves from air at normal incidence in the  $\pm 1$  diffraction orders. A 196.4 nm periodicity grating (50 nm height) was selected to create the evanescent waves and was added to the numerical model to predict the metamaterial's response to evanescent waves created by this approach. Conversely, placing a grating at the bottom of the structure, interfaced with vacuum, separates the evanescent and propagating transmission in the -1 and 0 diffraction orders, respectively. This is the scheme applied in far-field superlensing devices (Xiong et al., 2007a). Fig. 3.3 illustrates the design steps and shows how simple reflection is a convenient proxy to evaluate the

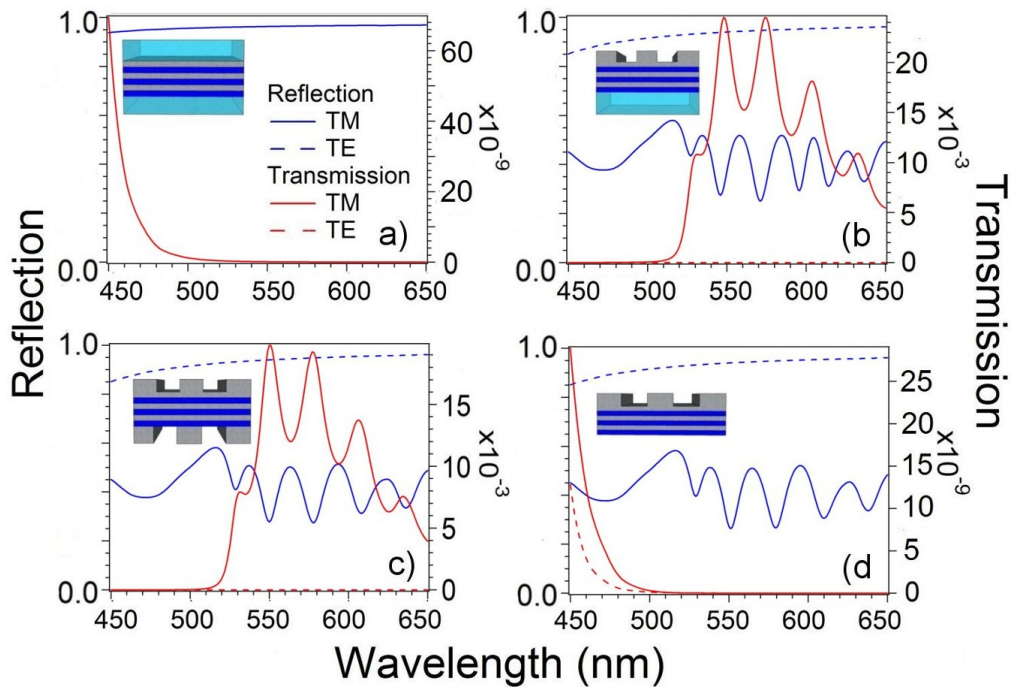


Figure 3.3: Reflection and Transmission simulations of white light at normal incidence on a multilayer. a) Light incident on the metamaterial from  $n = 4$  and transmitted into  $n = 4$ . b) White light incident on a diffraction grating in vacuum on a metamaterial transmitted into  $n = 4$ . c) White light incident on a diffraction grating on a metamaterial diffracted through a grating in vacuum (superlens configuration). d) White light incident on a diffraction grating in vacuum on a metamaterial transmitted into vacuum. Inset in each of the figures is a schematic of the metamaterial and its surrounding structures.

metamaterial potential performance. In Fig. 3.3a, even though the  $n = 4$  material can support waves with  $k_x \leq 4$ , there is no object to scatter waves with  $k_x \leq 4$  at normal incidence. The diffraction grating interfaced with vacuum in Fig. 3.3b scatters evanescent waves that are enhanced in the metamaterial by surface plasmons and transmitted into the  $n = 4$  material as evinced by the peaks in transmission and corresponding dips in reflectance. In Fig. 3.3c, a diffraction grating acts as scattering object to generate evanescent waves and the  $n = 4$  material is replaced with a grating on the transmission side to convert enhanced evanescent waves into propagating waves. Here also, I see the strong transmission peaks and reflectance dips. Finally, in Fig. 3.3d, I see that the performance of the metamaterial with a grating on the incident side and vacuum on the transmitted side exhibits a reflectance spectrum similar to the two grating case. Dips and peaks in Figs. 3.3a-d are due to evanescent wave coupling to surface plasmons as the TM polarization changes with the addition and subtraction of diffraction gratings, but the TE spectrum remains constant in the various configurations. The optical constants used in all the simulations were measured via spectroscopic ellipsometry from films fabricated in our laboratory, their values were found to be only slightly different from literature values. In particular, the oxide is amorphous with a refractive index approximately equal to 1.6 in the visible range.

I fabricated the designed metamaterial by depositing the  $\text{Al}_2\text{O}_3$  and Ag layers onto a glass substrate via pulsed laser deposition (PLD) with a KrF excimer laser operating at 248 nm, with pulse energy 300 mJ (pulse fluence  $\sim 1 \text{ mJ}/\text{cm}^2$ ), at 40 Hz followed by a 50 nm Ag layer for the grating. The deposition is smooth and large areas of the multilayer

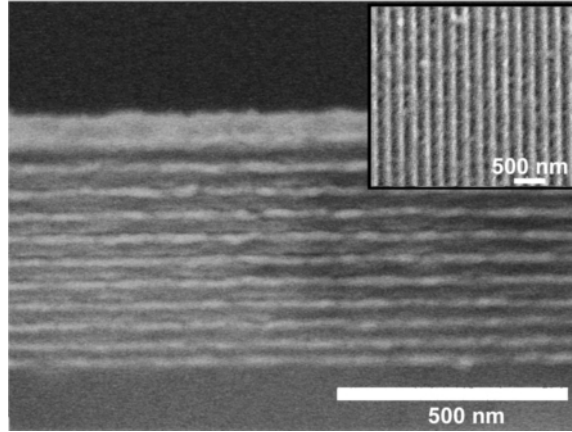


Figure 3.4: Scanning electron micrograph of the cross section of the metamaterial on glass with a 50 nm Ag layer before the grating milling. Inset, a top view zoom of the 196.4 nm periodicity grating in Ag.

appear free of defects by optical and electron microscope inspection. Finally, I used a focused ion beam to mill a  $19.64 \mu\text{m}$  by  $19.64 \mu\text{m}$  grating with 196.4 nm periodicity into the final Ag layer. Fig. 3.4 shows a cross section electron micrograph of the metamaterial with the 50 nm Ag layer on glass and a top view of the ion beam milled grating.

## 3.2 Experimental

I examined the reflection and transmission incident on the diffraction grating on the metamaterial using a Nikon bright field microscope and a broad spectrum white light source in a confocal configuration shown in Fig. 3.5. The incident beam was polarized to either TM or TE (with  $10^4$  extinction ratio). Using a 10x objective and restricting the numerical aperture with an iris on both the incident and reflected beams, I keep the light cone with an opening angle  $\sim 4^\circ$  to guarantee true normal incidence. The spot size was set by the optical fiber to approximately a  $15 \mu\text{m}$  diameter on the diffraction grating.

Fig. 3.5 presents the experimental and simulated reflection from the 1D grating and

metamaterial system for both the TM and TE polarizations. The TM polarization exhibits several oscillations across the visible due to excitation of the surface plasmons in the metamaterial. The large dip at the blue end of the spectrum is preferential absorption of the TM polarization by the metal grating and not the metamaterial (Yang and Lu, 2007) and is confirmed by simulation.

The diffraction grating generates evanescent waves with

$$k_x = \frac{2\pi m}{\Lambda} \quad (3.1)$$

where  $m = \pm 1$ . For  $\Lambda = 196.4$  nm the  $k_x$ -vector is  $0.032 \text{ nm}^{-1}$ , which ranges from  $2.04 \cdot k_0$  to  $3.56 \cdot k_0$  for  $\lambda$  from 400 nm to 700 nm. Inspection of the dispersion relation (Fig. 3.2) reveals that there are 6 intersections with  $k_x = 0.032 \text{ nm}^{-1}$ , which correspond to 6 dips in the reflection. These closely translate to the dips in the TM reflection spectrum in Fig. 3.5. The TE shows only a slight rise over the whole of the visible spectrum with its total reflection remaining close to 90 %. As the TE polarized evanescent waves do not couple to surface plasmons this is an expected result. Though the overall trends suggest correspondence to simulation, the TM reflectance dips do not lie perfectly at the expected frequencies from the dispersion relationship. The presence of the grating that is not included in that dispersion relationship calculation and some thickness variation among the layers could be the reason for such small differences. However, the most obvious difference between the experimental and modeled reflection curves is that the TM background line is approximately 46 % higher than predicted and the TE is 20 % lower than simulation. The amplitudes of the TM oscillations are smaller than simulation

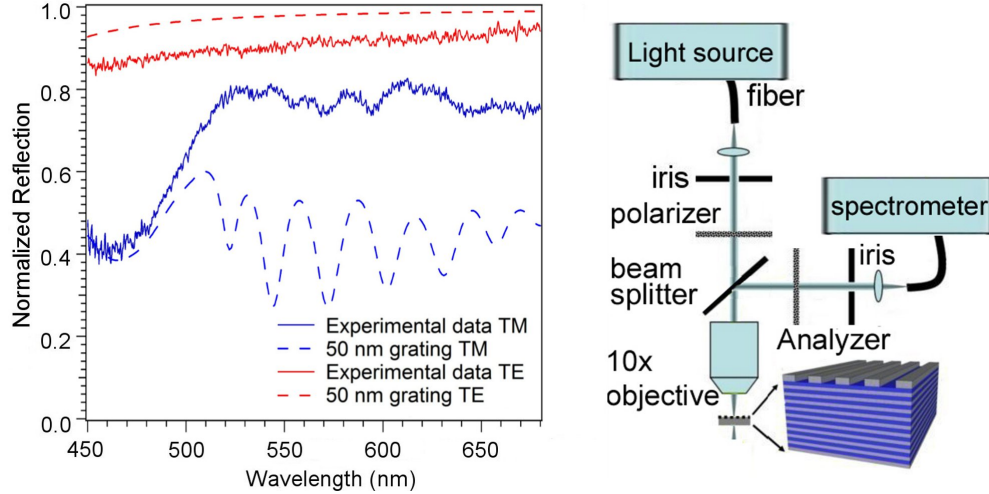


Figure 3.5: Experimental data for normalized reflection from a 196.4 nm periodicity grating on a 10 pair  $A_2O_3$  and Ag metamaterial with layer thicknesses of 29.5 and 27 nm, respectively with the simulated reflection for the case of a 50 nm high Ag grating. All values are normalized by the reflection from the metamaterial. Right: Diagram of confocal set-up from a 50  $\mu\text{m}$  fiber and 10x microscope objective.

by at least 40 %. It is worth noting, also, that for both polarizations, the experimental transmission curves increase in value from blue to red wavelengths while the simulated do not. None of the geometrical or material parameters were found to be potentially responsible for such deteriorated performance while I explored the parameter space in the numerical simulations.

Transmission measurements taken to help understand the reflectance results are presented in Fig. B.4. They exhibit no preferred polarization transmitted through the system which is consistent with simulations as there is no additional grating on the transmission side to convert surface plasmons to propagating waves. Also, independent of the polarization of the incident beam, there is significant depolarization. Light emerges with a polarization contrast two orders of magnitude smaller than the incident prepared beam. This suggests that the metamaterial structure presents a large amount of depolarization

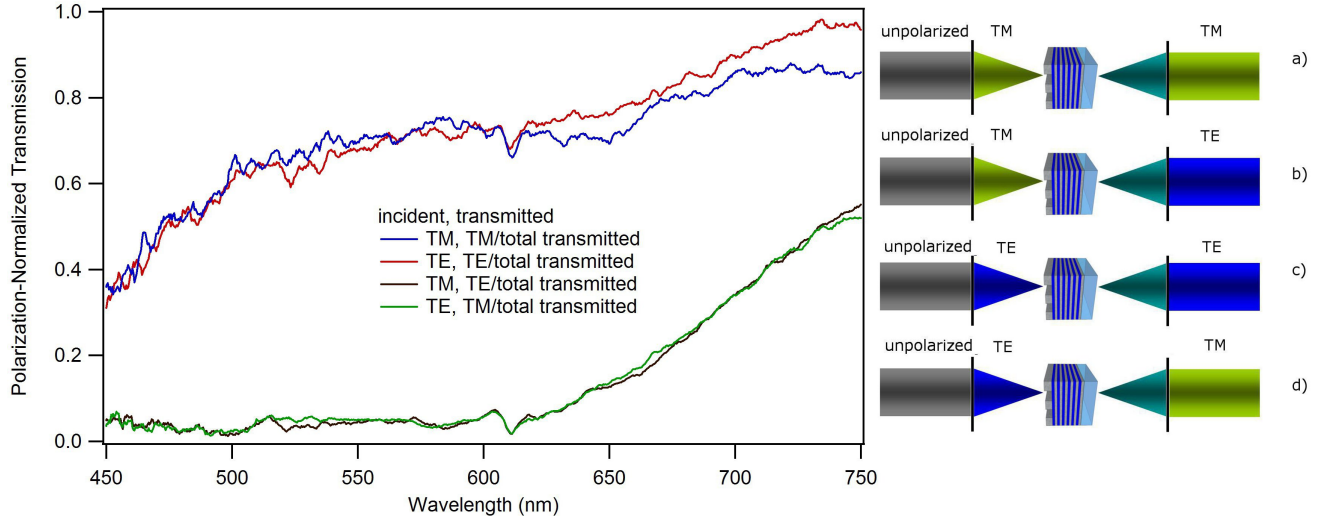


Figure 3.6: Left: Transmission enhancement of polarized and unpolarized light through the grating and metamaterial. Above are the polarized transmissions normalized by the total transmissions for TM and TE incident waves. Right: Simplified graphical representation of the polarized transmission. In each system, collimated, unpolarized light is linearly polarized and focused through an objective onto the sample, then transmitted light passes through a polarizer and is analyzed with a spectrometer. In a) incident light is TM polarized, measured transmitted light is TM polarized. In b) incident light is TM polarized, collected transmitted light is TE polarized. In c) incident light is TE polarized, collected transmitted light is TE polarized. In d) incident light is TE polarized, collected transmitted light is TM polarized. Images b and d are examples of cross-polarization.

which is likely deteriorating the plasmon waves and thus giving rise to the diminishing performance in reflection.

Likely sources of the unpolarized scattering are the surface roughness on the incident and transmitted surfaces of the metamaterial or the interface roughness between the  $\text{Al}_2\text{O}_3$  and Ag layers observed in Fig. 3.4. However, the scale of these roughnesses appears to be well under 2 nm, near 3 orders of magnitude smaller than the wavelengths involved. Although surface plasmon polaritons are well known to be highly sensitive to the quality of the interfaces, it appears that this sensitivity is heightened and/or multiplied by the number of interfaces involved.

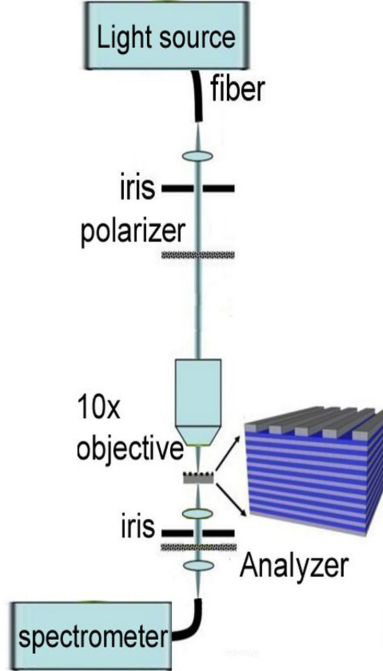


Figure 3.7: confocal arrangement for the transmission

### 3.3 Conclusions

I have discussed the process of optimizing, fabricating, and characterizing the optical properties of a metamaterial tuned to enhance evanescent waves in the visible via coupling to surface plasmons through a subwavelength diffraction grating. The optimized metamaterial has 10 pairs of  $\text{Al}_2\text{O}_3$ -Ag with 29.5 nm and 27 nm thicknesses, respectively. I found no unsurmountable intrinsic problem with Ag absorption to obtain large design transmission for  $k_x > k_o$  waves in a broadband over the visible. Polarized reflection from a 196.4 nm period grating placed on top of a fabricated metamaterial system followed the trends of the simulated reflection as well as those predicted by its dispersion relation calculation. However, both TM and TE reflection measurements presented exiguous performance. Transmission measurements exhibited signs of strong depolarization effects,

pointing to significant plasmon scattering inside the metamaterial. Possible causes of these phenomena are surfaces and interface imperfections, but I am unable to determine with certainty the cause of this effect. Beyond the intrinsic problem introduced from higher absorption by metals in the visible the fabrication imperfections seem to affect greatly the evanescent wave to surface plasmon coupling performance in an amplified fashion given the large number of interfaces involved.

This work was supported by the National Science Foundation Graduate Research Fellowship Program.

## CHAPTER 4

### CHARACTERIZATION OF TRANSMISSION SPECTRA THROUGH A METALLO-DIELECTRIC METAMATERIAL THIN FILM PERFORATED BY SUBWAVELENGTH CIRCULAR HOLE ARRAYS

#### **Abstract:**

Optically thick metallo-dielectric multilayer films perforated with a periodic array of sub-wavelength holes show exceptional transmission properties. The zero order transmission spectra exhibit well defined maxima and minima determined by the periodicity of the arrays. Despite possessing an expanded dispersion relation, the metamaterial exhibits transmission peaks at wavelengths very similar to those of a Ag thin film of equivalent thickness. Even though the metamaterial supports enhanced transmission several orders of magnitude larger than that of the Ag film in the range of evanescent waves created by the single apertures, the relative intensities of the transmission peaks for both metamaterial and Ag are similar, suggesting that the intensity of surface plasmons generated by the subwavelength holes is negligible compared to the intensity of those generated by the grating periodicity. Experimental and numerical simulations are presented to demonstrate this result.

In 1998 Ebbesen demonstrated that when an array of subwavelength circular holes in a thin metal film was illuminated with light, more light was transmitted through the holes than was incident on them. He coined the term extraordinary optical transmission (EOT)(Ebbesen et al., 1998). This work generated strong interest in the manipulation of light at subwavelength holes with artificial apertures (Degiron and Ebbesen, 2005; Grupp et al., 2000; Klein Koerkamp et al., 2004). They were studied for incorporation into optical computing systems, wavelength selective filters, multiplexers, and a variety of other uses. The mechanism behind this enhanced transmission is dependent on surface plasmons excited on the surface of the metal film. Light interacts with the subwavelength features exciting surface plasmons related to the periodicity, hole size, and in some cases, shape. While the subwavelength aperture is too small for the incident propagating light to penetrate, the surface plasmons, which have high resolution capabilities, tunnel from one side of the aperture to the other and effectively couple the incident and transmitted surfaces. The quantity used to define this is the absolute transmission efficiency (ATE) which is the zero-order normalized transmission through the apertures divided by the fraction of area in the incident beam cross-section occupied by the holes, themselves. The surface plasmons excited on the surface of the metal not occupied by the holes are able to contribute to the zero order transmission on the other side of the film, breaking the classical aperture transmission limit with an ATE greater than 1 for resonant wavelengths.

As mentioned previously in section 1.6, surface plasmons are characterized by having a longer momentum vector than the free space light cone. For the purposes of this study, I

will examine the k-vectors along the surface of the thin film in the x-direction. The longer momentum vectors mean that the surface plasmon probes into the subwavelength aperture where light cannot reach due to the diffraction limit. Their resonant excitation from a free wave requires momentum exchange at the surface of the thin film. In an aperture array, the periodic structure acts as a diffraction grating and shifts the momentum of the propagating light to longer k-vectors to excite the surface plasmon at selected wavelengths (Ghaemi et al., 1998; Lezec et al., 2001). Here, in EOT, there is a large transmission peak at the resonant wavelength of the excited oscillation.

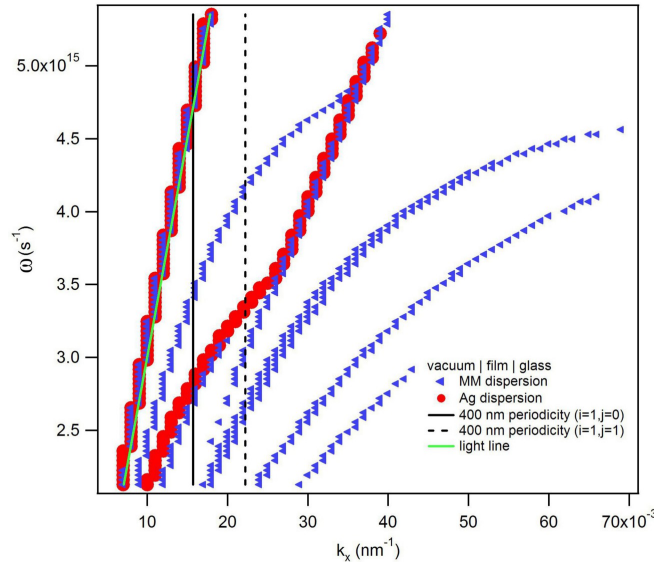


Figure 4.1: Calculated dispersion curves of the four pair  $\text{Al}_2\text{O}_3$ -Ag metamaterial on glass (blue triangles) and an equivalent 80 nm thick Ag film (red circles) as a function of parallel momentum vector. The solid green line is the vacuum light cone, the solid black line is the fourier transform of the 400 nm periodicity ( $i=1, j=0$ ),  $0.0157 \text{ nm}^{-1}$ , and the black dashed line is the fourier transform of the 400 nm periodicity ( $i=1, j=1$ ),  $0.0222 \text{ nm}^{-1}$ .

The typical EOT spectrum also presents transmission minima that are attributed to a non-resonant Wood's anomaly in which the diffracted order becomes parallel to the interface and the intensity is redistributed amongst the other orders, leading to a sharp

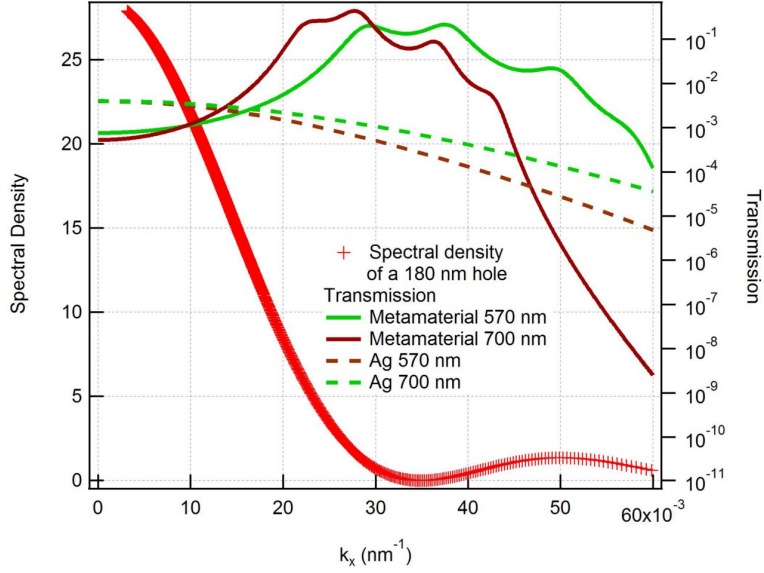


Figure 4.2: Simulated TM polarized transmission through a metamaterial (solid curves) and a Ag (dashed curves) thin film embedded in an  $n = 8$  material overlaid by the spectral density of a 180 nm diameter hole as a function of  $k_x$  at 700 nm (brown) and 570 nm (green) incident wavelength.

drop in zero-order transmission.

$$\lambda_W = \frac{\Lambda}{\sqrt{i^2 + j^2}} \sqrt{\epsilon_d} \quad (4.1)$$

where  $\Lambda$  is the periodicity of the hole array,  $\epsilon_d$  is the permittivity of the dielectric on one side of the interface, and  $i$  and  $j$  are integers.

Another feature is the band gap of the periodic structure relating to the spatial distribution of the electric field in the illuminated area. The combination of this plasmon-polariton coupling with the Wood's minima and band gap successfully explains the key features of the EOT in noble metal thin films punctured with arrays of nanoapertures.

In the last decade, studies of this system have examined the role of film thickness, type of metal, periodicity, as well as hole shape on extraordinary transmission for possible

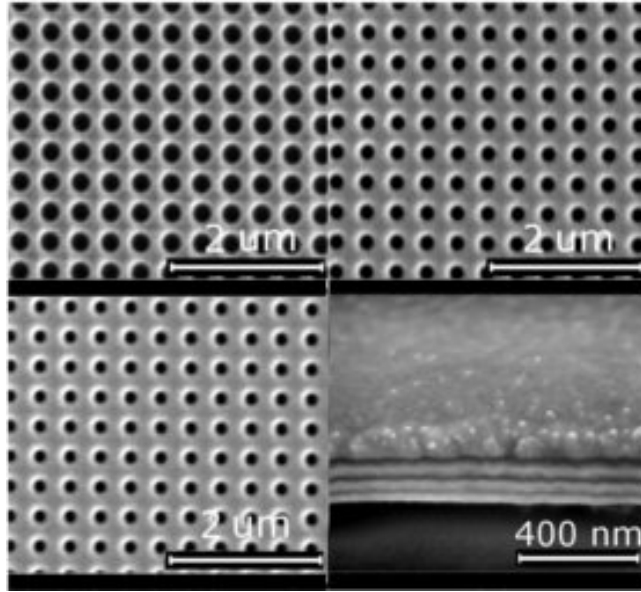


Figure 4.3: Electron micrographs of the periodic hole arrays in the metamaterial. Top Left: normal incidence view of the 250 nm diameter holes. Top Right: normal incidence view of the 180 nm diameter holes. Bottom Left: normal incidence view of the 150 nm diameter holes. Bottom Right: Cross section view of the metamaterial at 52 °.  $\text{Al}_2\text{O}_3$  is the top layer.

uses as optical tuners and near field optical components(Klein Koerkamp et al., 2004; van der Molen et al., 2005; Chang et al., 2005; Kim et al., 1999). More recently, interest has been rising in the application of metamaterials as a way to reduce the losses associated with plasmon-polaritons based structures. Metallo-dielectric metamaterials, comprising alternating layers of metal and dielectric with subwavelength thicknesses, are films whose evanescent wave transmission is greatly enhanced. They have been used to mitigate evanescent wave decay by coupling to plasmon-polariton waves with a less lossy interaction(Wood et al., 2006). The metamaterial satisfies the physical requirement of negative permittivity to support surface plasmons but has fewer losses than metals. Surface plasmons are excited at each of the multilayer interfaces instead of just at the incident and transmitted surfaces as in a simple one layer metal film. These couple to modify the

position of the resonance, expand the number of supported surface plasmon modes, and increase the transmission of high k-vector waves. Metamaterials can be tuned to support a large band of long momentum wave vectors across the visible and allow transmittances several orders of magnitude larger than those of a single metal film of overall equivalent thickness. The resonance position and interference of these surface plasmons are adjusted by the metal-dielectric thickness ratio that tunes the permittivity tensor and controls the overall optical properties (Xiong et al., 2007a) via the following equations:

$$\epsilon_x = \frac{\epsilon_{metal} + \eta\epsilon_{dielectric}}{1 + \eta} \quad (4.2)$$

and

$$\frac{1}{\epsilon_z} = \left( \frac{1}{\epsilon_{metal}} + \frac{\eta}{\epsilon_{dielectric}} \right) (1 + \eta) \quad (4.3)$$

where  $\epsilon_x$  is the transverse permittivity component along the interface in the x-direction,  $\epsilon_z$  is the longitudinal permittivity component,  $\eta$  is the dielectric to metal ratio. As the ratio increases, the metamaterial becomes more dielectric-like, and as it decreases, it becomes more metal-like.

EOT in metamaterial structures remains relatively unexplored. Given their documented ability to improve optical transmission over single metal films, it is the expectation that they could prove better or show significantly different performance than their single metal layer counterparts. It is not known yet if the presence of holes in the metamaterial will decrease the coupling of the surface plasmons at each interface. Here, I show that such expectations are not directly fulfilled and indicate further challenges to

fabricate structures that exploit the enhanced transmission of metamaterials. I present a characterization and comparison of the EOT of visible light through a thin film  $\text{Al}_2\text{O}_3$ -Ag metamaterial and an equivalent thickness Ag film perforated by a 400 nm periodicity array of subwavelength circular holes with varying aperture diameter. Though the dispersion relation and long momentum vector propagations are drastically different from those of the Ag film, the metamaterial transmission spectrum exhibits the same trends as the Ag thin film with a slight red shift. The transmission peaks also exhibit similar maximum values to those of the transmission spectrum of the Ag film. Experimental extraordinary transmission through the arrays aligns well with the simulations but has a somewhat diminished response. I show that though the propagation of large-momentum waves in the metamaterial is several orders of magnitude higher than in the Ag film, the surface plasmons generated in this region by the hole sizes are negligible compared to those generated by the periodicity of the diffraction grating, and the spectral responses of the metamaterial and Ag films are essentially the same.

## 4.1 Fabrication and Spectral Response

The metamaterial that is the subject of this study consists of a four-pair  $\text{Al}_2\text{O}_3$ -Ag multilayer with thicknesses of 20.0 nm each. The light dispersion relationships of the metamaterial and single Ag layer on glass were calculated using the matrix formalism developed by Davis and is shown in Fig.4.1. It can be seen that both the Ag film and the metamaterial support surface plasmon modes outside the green free space light cone where a resonant transmission can be excited. The fourier response of the arrays in the

thin film will be the convolution of a single subwavelength aperture and a periodic array of delta functions. The 400 nm periodicity parallel momentum vector line crosses the Ag surface plasmon mode at  $\lambda = 690$  nm ( $\omega=2.73 \times 10^{15}$  s $^{-1}$ ) and two of the metamaterial modes at 570 nm ( $\omega=3.3 \times 10^{15}$  s $^{-1}$ ) and 698 nm ( $\omega=2.7 \times 10^{15}$  s $^{-1}$ ). I expect to see a strong transmission peak at each of the crossings launched from the periodic structure. This coupling is quantified by

$$\mathbf{k}_{\text{sp}} = \mathbf{k}_x + i\mathbf{G}_x + j\mathbf{G}_y \quad (4.4)$$

with  $\mathbf{k}_x = \hat{x} \frac{2\pi}{\Lambda} \text{Sin}(\theta)$  and  $G_x = G_y = \frac{2\pi}{\Lambda}$ . Here,  $i$  and  $j$  are integers,  $\theta$  is the light incident angle, and  $\Lambda$  is the periodicity. For the ( $i=1, j=1$ ) order, there is a crossing in the visible with Ag at the glass interface near  $\lambda = 570$  nm ( $\omega = 3.3 \times 10^{15}$  s $^{-1}$ ) and the metamaterial mode at  $\lambda = 449$  nm ( $\omega = 4.2 \times 10^{15}$  s $^{-1}$ ).

I have also calculated the optical transmission as a function of parallel momentum vector for the metamaterial and Ag films. This describes the relative intensity of response to long k-vector waves within the thin film. To calculate the transmission values for different  $k_x$ , 700 nm and 570 nm TM polarized light was launched from a high refractive index material ( $n = 8$ ) into the metamaterial or Ag film and was transmitted into the same high refractive index media at a variable incident angle resulting in  $k_x = n^* \left(\frac{2\pi}{\lambda}\right) \text{Sin}(\theta)$ . The results shown in Fig. 4.2, illustrate that even though the integrated silver thickness is the same in the two devices, the designed metamaterial is expected to have several orders of magnitude better transmission than the single layer Ag film in a broad range of long k-vector waves. Overlaid on the enhanced transmission figure is the spectral density of a subwavelength hole (the square of its Fourier transform divided by the diameter of the

hole)(Born and Wolf, 2002). It can be observed that the reciprocal space description of the subwavelength aperture limits the spectral content of the hole array to wavenumbers  $\leq 0.030 \text{ nm}^{-1}$ . Nevertheless, there is significant spectral content that overlaps the regions of enhanced transmission in the metamaterial, particularly around the wavevectors associated with the periodic structure. The structure should allow coupling to higher k-vector waves, including surface plasmon polaritons, that propagate with reduced attenuation in the metamaterial. As a result, I would expect hole arrays in the metamaterial to have higher transmission than similar arrays in a silver film.

I fabricated the metamaterial by depositing the  $\text{Al}_2\text{O}_3$  and Ag layers of 20.0 nm thickness onto a glass substrate via pulsed laser deposition (PLD) with a KrF excimer laser operating at 248 nm, with pulse energy 300 mJ (pulse fluence  $\sim 1 \text{ J/cm}^2$ ), at 40 Hz with Ag as the first deposited layer. The film is smooth and large areas of the multilayer appear free of defects by optical and electron microscope inspection. Finally, I used a focused ion beam to mill  $7.6 \mu\text{m} \times 7.6 \mu\text{m}$  arrays of cylindrical holes with 400 nm periodicity and hole diameters of 250 nm, 180 nm, and 150 nm through all the layers. Fig. 4.3 shows the three arrays and a cross section view of the metamaterial. The Ag films were deposited with PLD and arrays milled with the focused ion beam under the same parameters listed above.

## 4.2 Experiment and Simulation

I examined the zero-order transmission from illumination of the subwavelength arrays in the metamaterial using a Nikon bright field microscope and a broad spectrum white light

source in a confocal configuration. Using a 10x objective and restricting the numerical aperture with an iris on the incident beam, I keep the light cone to an opening angle  $\sim 4^\circ$  to maintain conditions close to true normal incidence. Fig.4.5 provides a diagram of the microscope configuration used.

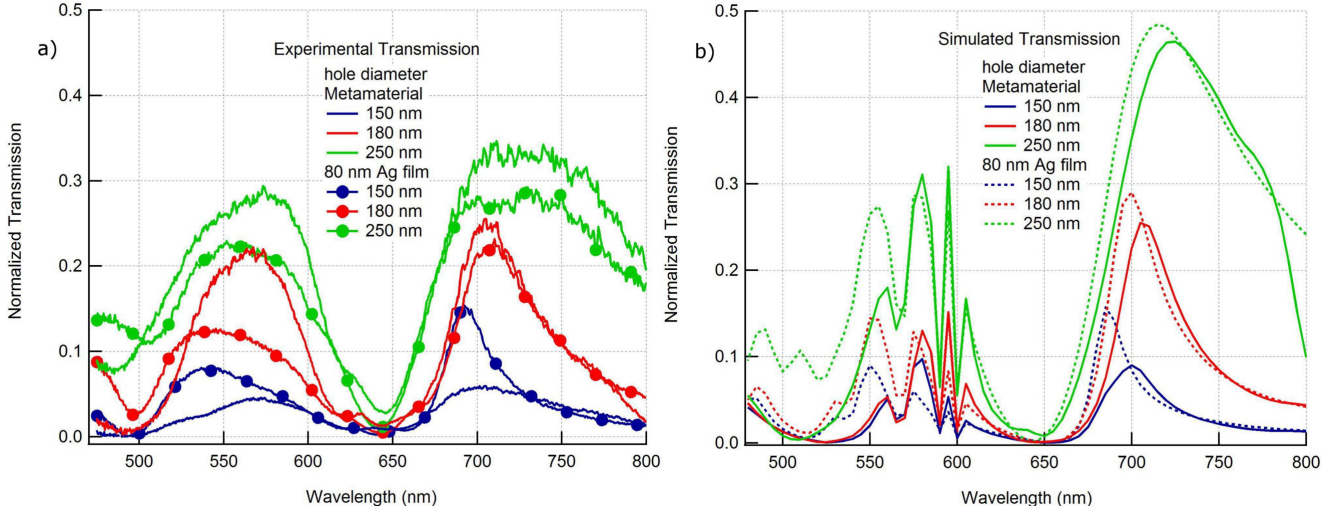


Figure 4.4: Normalized transmission vs wavelength for hole arrays of 250 nm (green), 180 nm (red), and 150 nm (blue) diameter. Shown are the a) experimental and b) simulated curves for the metamaterial and an equivalent Ag film of 80 nm thickness.

Fig. 4.4a presents the experimental transmission curves for the 250 nm, 180 nm, and 150 nm diameter hole arrays in the metamaterial and the equivalent Ag film with 80 nm thickness. I can observe that in both devices, the 250 nm diameter holes have the highest transmission followed by the 180 nm and 150 nm diameter holes. I also see that all spectra have peaks near 700 nm and 570 nm and a dip at 640 nm. The large dip at 640 nm is the band gap where no transmission is allowed. On the high energy side of the gap, the electric field is concentrated in the film material and on the low energy side, it is concentrated in the holes themselves (deCeglia et al., 2011). Though the metamaterial has additional surface plasmon modes, it is reasonable that it shares a band gap with the

Ag film because the gap wavelength is determined by the grating periodicity that excited their shared plasmon mode indicated in Fig.4.1.

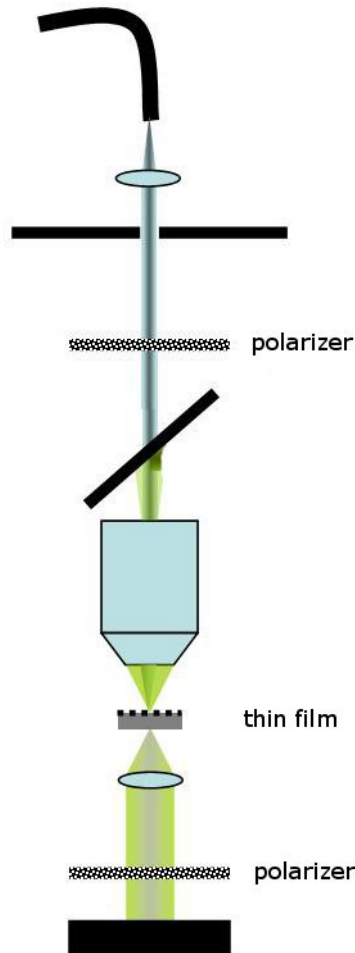


Figure 4.5: A diagram of the microscope set-up. White light enters from a fiber, is collimated and passes through a lens to restrict its numerical aperture. It is polarized before reaching the 10x microscope objective where it is focused on the surface of the hole array. Transmitted light is collimated with a lens and polarized before reaching the spectrometer.

Another noticeable feature in the spectra is the transmission peaks at the right and left of the minima. They are the result of the crossing of the periodicity with a supported surface plasmon mode as noted in the dispersion curve at  $(0.0157\text{nm}^{-1}, 3.3\text{e}15 \text{ s}^{-1})$  and  $(0.0222\text{nm}^{-1}, 2.7\text{e}15 \text{ s}^{-1})$ . This type of crossing is called a Rayleigh peak and is roughly

described by the equation:

$$\lambda_R = \frac{\Lambda}{\sqrt{i^2 + j^2}} \sqrt{\frac{\epsilon_d \epsilon_m}{\epsilon_d + \epsilon_m}} \quad (4.5)$$

where  $\epsilon_m$  is the permittivity of the thin film. The Rayleigh peaks near 700 nm and 570 nm are visible from the crossings of the glass surface plasmon mode of the (i=1,j=0) and the (i=1,j=1) periodicity lines, respectively. The similarity of the peak positions, despite the varying dispersion curves, arises from the various crossings with the (i=1,j=0) line with the shared plasmon mode and the (i=1,j=1) crossing with the Ag glass mode. Our spectral range and periodicity admit only this region of similarity to be viewed.

It is remarkable how close all the different silver and metamaterial spectra are at all hole sizes in terms of features and absolute transmission magnitudes in the explored range. Full electromagnetic simulations were performed afterwards using finite difference time domain algorithms to seek support for these observations. Finite-difference time-domain (FDTD) simulations were performed using commercial software (Lumerical's FDTD Solutions, v7.0.1) on a single workstation with 24 GB RAM (Dell Precision, Windows 7 Professional OS). Each simulation was run in parallel mode to utilize all eight 2.27-GHz cores of the two Intel Xeon quad-core processors, taking up 2.5 GB RAM and 11 hours to complete 500 fs ( $2.62 \times 10^5$  iterations) of simulation time, plus additional two hours for the near-to-far-field grating calculations. The simulation domain spanned an xyz-volume of  $400 \times 400 \times 2500$  nm<sup>3</sup>. Each experimental hole array was modeled as a repeating unit cell with dimensions of  $400 \times 400$  nm<sup>2</sup> in the xy-plane and a centered cylindrical hole of 150/180/250 nm diameter extruded through the (stack of) film(s) in the z-direction; anti-symmetric (along the polarization direction of the light source), symmetric, and perfectly-

matched-layers conditions were respectively applied at the x-, y-, and z-boundaries of the simulation domain. The (anti-)symmetric conditions behave as periodic boundaries but reduce the computational burden to 1/4 of the full unit cell. The domain was meshed globally with a non-uniform conformal grid, which was overridden locally, in a volume fully enclosing the hole-array unit cell, with a finer uniform grid of 1 nm step size. The unit cell was bounded along the z-direction by vacuum ( $n = 1.0$ ) on the input side and glass ( $n = 1.5$ ) on the output side. The white-light excitation source was an x-polarized plane wave at normal incidence, injected from the vacuum side as a broadband pulse of 4.65 fs temporal width and 350-900 nm spectral bandwidth. Planar power monitors were placed on opposite sides of the film(s) to calculate the fractions of the incident intensity transmitted and reflected into the zeroth grating orders. Material dispersion curves were obtained within the software by multi-coefficient fitting to ellipsometric data for the optical constants of the Ag and Al<sub>2</sub>O<sub>3</sub> films measured in our laboratory. These results are shown in Fig. 4.4b. The simulated curves match qualitatively with the experimental ones, but have a larger overall transmission. The diminished response of the experimentally obtained data has been reported to result from interface roughness introduced during the deposition process, even on the scale of 2 nm rms as the surface plasmons are highly sensitive to this scattering and depolarizing effect (Ray and Lopez, 2011). Nevertheless, I have also found very close resemblance between the metamaterial and single layer Ag transmittance. This, unfortunately, points to a negligible contribution from the coupled plasmons from the single aperture hole contribution. Another way to quantify these facts is the absolute transmission efficiency (ATE) calculated as the normalized zero-diffraction-

order transmission divided by the fraction of area in an array occupied by the holes. It measures the ratio of normal light transmitted through the holes to light incident on the holes and is predicted classically to scale as  $(d/\lambda)^4$  (Bethe, 1944). Table A.5 lists the maximum ATE calculated for the experimental transmission of the metamaterial and Ag films for the 700 nm peak and the 570 nm peak for each hole diameter. Values greater than unity signify that there is more light transmitted through the holes than is incident on them due to the excitation of surface plasmons on the films. All the values are well above classical prediction (which scales as  $10^{-4}$ ,  $10^{-4}$ , and  $10^{-3}$  for the 150 nm, 180 nm, and 250 nm diameter holes, respectively), but do not show significant differences between the two material structures tested.

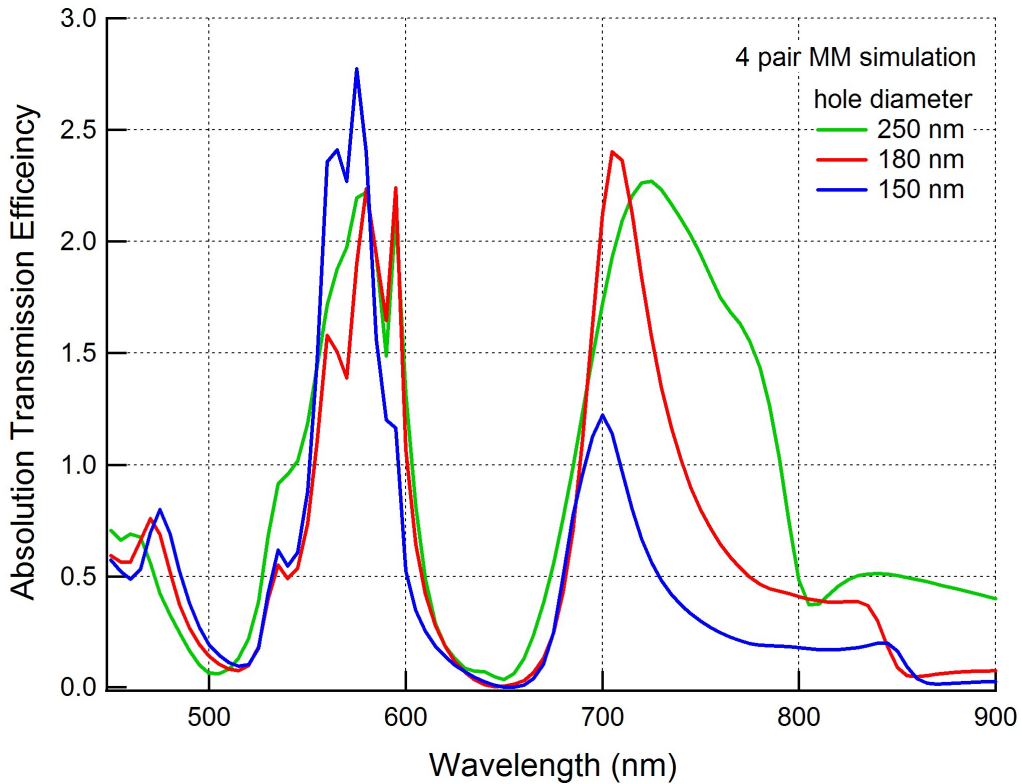


Figure 4.6: Absolute transmission Efficiency vs. wavelength for a 4 pair Ag-Al<sub>2</sub>O<sub>3</sub> metamaterial with 20 nm thicknesses, respectively. Periodicity is 400 nm with hole diameters of 250 (green), 180 (red), and 150 (blue) nm.

Table 4.1: Experimental Absolute Transmission Efficiency

150 nm	180 nm	250 nm	peak	film
0.53	1.55	1.04	700 nm	MM
1.34	1.40	0.90	700 nm	Ag
0.53	1.40	0.95	570 nm	MM
0.73	0.80	0.73	570 nm	Ag

### 4.3 Conclusions

In summary, the transmission spectrum of a 4 pair  $\text{Al}_2\text{O}_3$ -Ag metamaterial with thicknesses of 20.0 nm, each, perforated by subwavelength hole arrays is similar to that of an equivalent perforated Ag thin film despite their differing dispersion curves and enhanced transmission for the non-perforated metamaterial film with respect to the non-perforated Ag film. Both sets of spectra exhibit a band gap dip at 640 nm, and Rayleigh peaks from the crossing of the  $(i=1, j=0)$  and  $(i=1, j=1)$  periodicity lines and the plasmon modes near 570 nm and 700 nm. While simulation reveals that the metamaterial transmission at long k-vectors is several orders of magnitude larger than the Ag film, this does not contribute to dramatically enhanced transmission through the metamaterial hole arrays because the accessible range of higher k-vector waves remains insufficient. It is perhaps possible to produce an enhanced EOT through a metamaterial but it will require an additional nanostructure capable of creating a greater density of plasmon polaritons than the single aperture holes.

This work has been supported by the National Science Foundation Graduate Research Fellowship.

## CHAPTER 5

### PLASMON MEDIATED ABSORPTION IN ORGANIC BULK HETEROJUNCTION SOLAR CELLS

#### **Abstract:**

Organic bulk heterojunction solar cells with subwavelength patterning of metallic layers that can produce surface plasmon polaritons have been shown to exhibit increased efficiency over their nonpatterned counterparts. Several mechanisms that could explain this enhancement have been suggested. I fabricate a Poly(3-hexylthiophene:[6,6]-phenyl C61-butyric acid methylester (P3HT:PCBM)-based inverted organic bulk heterojunction (BHJ) solar cell with a hexagonal diffraction grating with 400 nm post to post distance on the back Ag contact to excite surface plasmons. From the dispersion relation of the active region-cathode interface I identify an excited surface plasmon from the grating at 680 nm. The patterned cell has an open circuit voltage ( $V_{oc}$ ) and short circuit current ( $J_{sc}$ ) of 0.6 V and 9 mA/cm<sup>2</sup>, respectively, giving it a 60 % increase in  $J_{sc}$  over the flat cell fabricated with the same material proportions and fabrication procedures. In order to explain this enhancement, I analyzed the characteristics of the cells. The incident photon to electron conversion efficiency (IPCE) curves of the patterned cell have peaks at 480 nm and 600

nm and none at the predicted plasmon coupling, 680 nm. I show that these peaks are due to the increased light path resulting from diffraction and not to the localized electric field from surface plasmons, by varying the incident angle of the absorbed light.

Global energy consumption has been doubling about every 40 years with less than 10 % of this energy currently comes from renewable sources(Perez-Lombard et al., 2008). Among sustainable resources is sun light that can be converted to electrical current by photovoltaic devices. Silicon has been the material of choice used to fabricate solar cells because of its relatively good optical properties and its availability. However, the prospect of cost reduction has fueled recent research into organic solar cells, which are less expensive to fabricate, but so far, less efficient. Many techniques to increase the efficiency of organic solar cells have been investigated. Recently, the introduction of plasmonic structures has been shown to increase the optical absorption and the IPCE(Kim et al., 2008; Kume et al., 1995; Morfa et al., 2008; Lindquist et al., 2008). However, little is understood about the origin of this enhancement. It has been suggested that the increase in absorption is due to the localized electric field created by surface plasmons in the vicinity of the patterned interface(Atwater and Ablert, 2010; Tvingstedt et al., 2007; Min et al., 2010; Wang et al., 2010). The enhanced field could result in more light absorption, leading to more exciton creation. However, subwavelength structures can also simply scatter light in the active layer, lengthening the interaction path of incident photons within the absorbing material(Na et al., 2008; Niggemann et al., 2004). The longer the path length in the

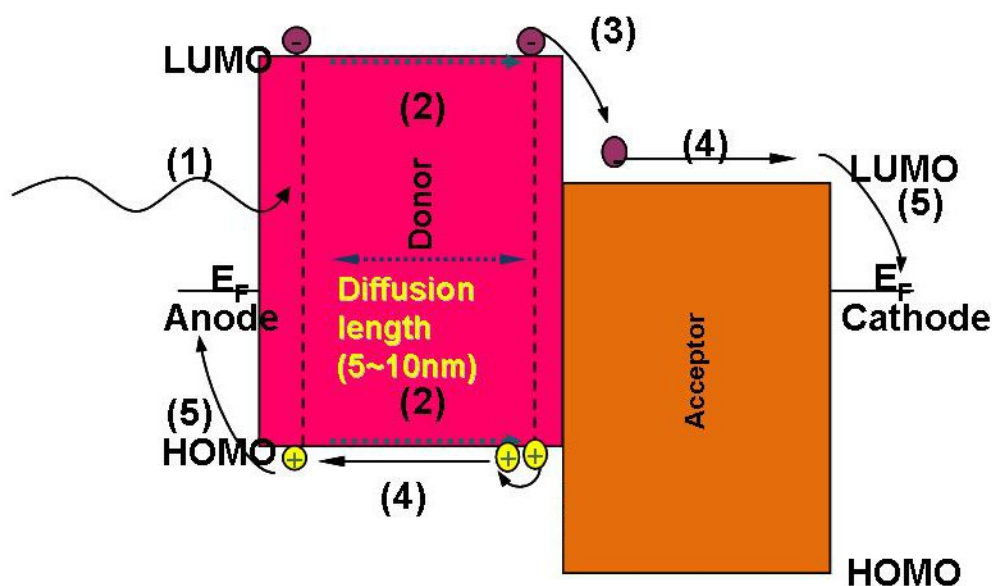


Figure 5.1: Graphical representation of the photovoltaic process in an organic BHJ solar cell. 1) the photon penetrates the active layer, 2) the absorption of a photon creates and exciton, 3) the exciton dissociates with the movement of the electron to the acceptor 4) a current is generated

active layer, the larger the absorbing cross section and the more excitons can also be generated. I seek to separate these two absorption mechanisms to further understand the physical processes governing the interaction of light with organic solar cells.

The BHJ materials are a mix of electron donor and electron acceptor organic components that phase-separate into nanoscale domains ( $\sim 15$  nm) distributed throughout the active layer. The materials are mixed together in solution and incorporated into the cell. When light penetrates to these active layers, photons excite electron-hole pairs bound together, called excitons, which then diffuse to the interface between the donor and acceptor material. After dissociation at the interface, the electron moves to the LUMO of the acceptor. The hole and electron then move to their associated electrode to become an electrical current. There are many processes governing this conversion such as diffusion

length, absorption cross section, thermal and potential barriers, recombination, etc. I will not discuss them in detail but will briefly cover the optimizations leading to our current configuration. The benefit that the BHJ structure brings to the photovoltaic system is the distribution of the interface throughout the active layer to accommodate the short diffusion length of the exciton by bringing the interface as close as possible to a generation point. As discussed above, the introduction of a plasmonic structure to this device is thought to create surface plasmons and/or increased light scattering throughout the cell.

In this chapter I characterize an inverted BHJ organic solar cell with a hexagonal grating (400 nm characteristic length) patterned on its back cathode. I show that there is an increase in the short circuit current over a flat reference cell and that the maximum-normalized IPCE shows a peak at 600 nm where the absorption of the flat cell drops off. While this peak agrees well with the simulated optical absorption and is enhanced over the reference cell, a predicted plasmonic peak near 700 nm is not present. Investigation of the IPCE as a function of angle exhibits no shift in position with changing incident  $k_T$  component of the propagation vector, leading to the conclusion that at least in this instance, there are no significant contributions to the electrical performance from the generation of surface plasmons. The increase in IPCE at 600 nm is then shown to be due to the refractive index of the P3HT:PCBM active layer that is nonuniform across the visible and to the increase in path length induced by scattering

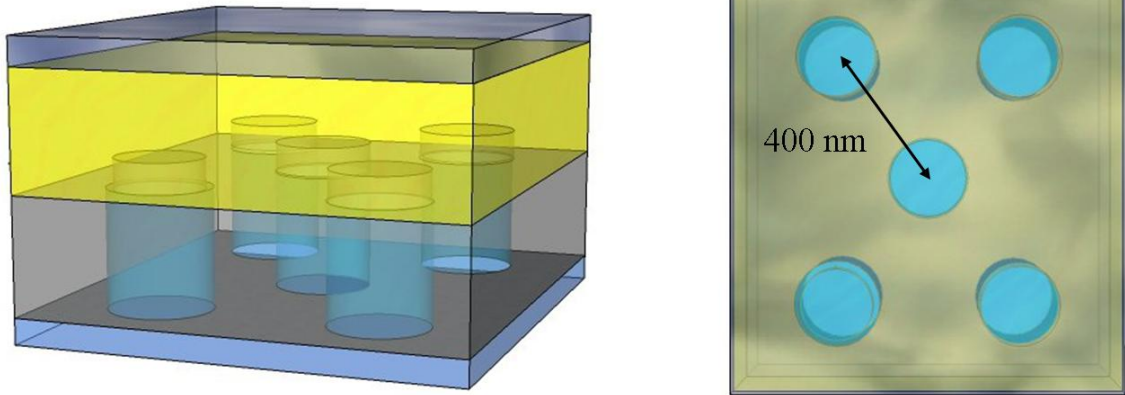


Figure 5.2: Graphical representation of the inverted solar cell with patterned cathode. Visible from bottom to top are the glass substrate, an array of SU8 pillars, a coating of Ag resulting in an Ag diffraction grating, followed by the active layer P3HT:PCBM with a top transparent anode.

## 5.1 Fabrication

I fabricated the inverted solar cell using SU-8 photoresist patterned on a glass substrate with nanoimprinting to form a hexagonal array of 200 nm by 200 nm pillars with 400 nm spacing. Then, I thermally evaporated 200 nm of Ag on the substrate to form a diffraction grating following the trends of the SU8 pillar array with substantially reduced height. This Ag layer also has enough thickness to act as a bulk film cathode and to support surface plasmons. Using pulsed laser deposition with 300 mJ, 25 Hz (pulse fluence  $\sim 1$  mJ/cm<sup>2</sup>), and a background O<sub>2</sub> pressure of 10 mTorr, I deposited 5 nm of ZnO doped with 2 % Al<sub>2</sub>O<sub>3</sub> to aid wetting of the Ag surface with the active layer. I made a P3HT:PCBM solution 1:1 by mass dissolved in chlorobenzene. I then spincoated 130  $\mu$ L on the Ag coated substrate at 1000 rpm for 90 s. The top contact of 10 nm of WO<sub>3</sub> and 10 nm Au was thermally evaporated onto the cell.

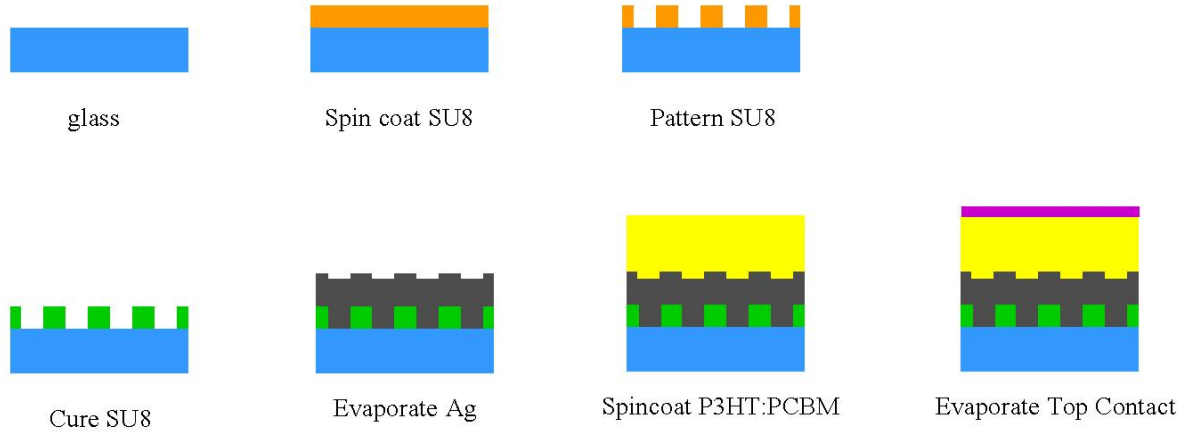


Figure 5.3: Graphical steps of the inverted solar cell fabrication process.

## 5.2 Electrical Characterization

Current-voltage measurements were taken under 1 sun illumination to measure photocurrent. Fig.5.4 shows the current-voltage measurements taken for a flat reference cell with no diffraction grating and those from a patterned inverted cell. The patterned cell has a  $J_{sc}$  equal to  $9.6 \text{ mA/cm}^{-2}$  and a  $V_{oc}$  of 0.6 V. The flat cell was fabricated in parallel following exactly the same steps but excluding the SU8 layer. It shows a  $J_{oc}$  of  $5.8 \text{ mA/cm}^{-2}$  and a  $V_{oc}$  of 0.6 V. Also, the patterned cell has a larger fill factor (0.35) and efficiency (1.68 %) than the flat cell (0.2 and 0.58 %).

While the I-V curves demonstrate the superior electrical performance of the patterned cell, they provide no means to decouple the effects of diffraction and plasmon generation. The IPCE, however tends to follow the optical absorption trends and measures the fractional contribution to total current generation as a function of wavelength. If the surface plasmon contributes to the efficiency, there should be a peak in the IPCE at the predicted coupling wavelength. In the inverted solar cell, there will be a surface plasmon generated

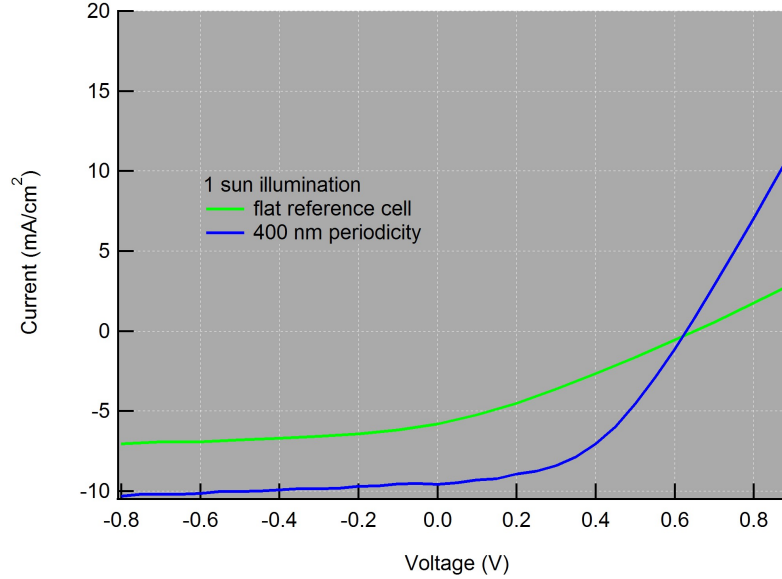


Figure 5.4: I-V curves under 1 sun illumination for a patterned cell (blue) and a flat reference cell (green).

at the P3HT:PCBM-Ag interface due to the periodicity of the diffraction grating. Fig.5.5 is the calculation of the dispersion curve the light cone (black), P3HT:PCBM (red), and the surface plasmon mode supported at the active layer-Ag interface (blue). Also present are the transverse momentum values generated by the diffraction grating for the (1,0) and (1,1) orders (dotted and dashed blue). A surface plasmon is generated when the grating momentum crosses a plasmon mode. In the visible, a crossing occurs at 680 nm ( $k_T=0.0222 \text{ nm}^{-1}$ ,  $\omega=2.8e15 \text{ Hz}$ ), which should be visible in the optical absorption and the IPCE.

I isolate which spectral region has the highest contribution to current production, by normalizing the IPCE vs. wavelength to its maximum value. Fig.5.6 compares the results for a flat reference cell and the patterned cell. The flat cell has its maximum IPCE value at 530 nm where P3HT:PCBM is strongly absorbing and there is a peak in the solar spectrum intensity. For the patterned cell, the increased electrical performance comes

from two peaks, at 490 nm and 600 nm, and the shoulder on the red side of the 600 nm peak. Notably, there is no IPCE peak at the plasmon excitation 680 nm.

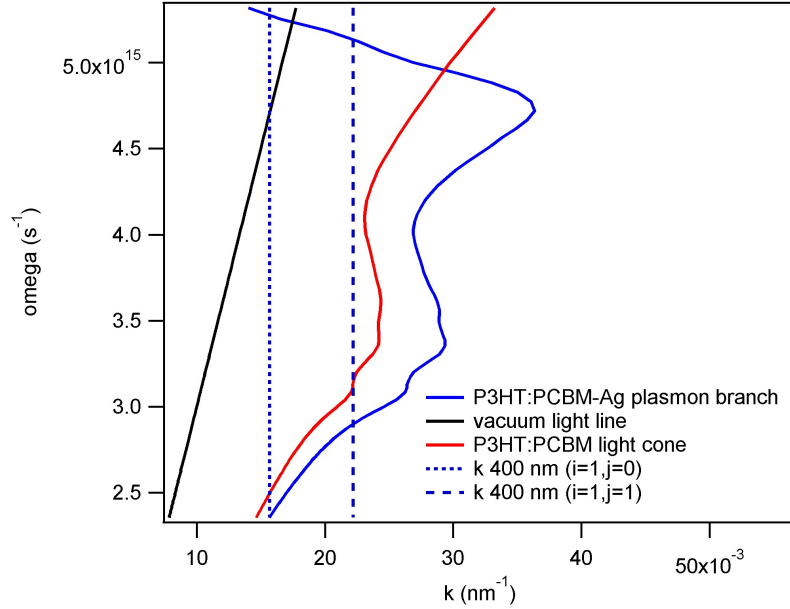


Figure 5.5: Dispersion curves for the free space light line (black), the P3HT:PCBM light line (red), and the surface plasmon mode at the P3HT:PCBM-Ag interface (blue).

### 5.3 Plasmonic Isolation

The behavior of the IPCE peaks under variation of the incident angle also helps to differentiate their production mechanisms. Under rotation of  $\theta_i$ , the peaks due to scattering will not change position, but the surface plasmon peaks will redshift. Changing the incident angle alters the momentum as  $k_T = m2n\pi\text{Sin}(\theta_i)/(n\Lambda)$ , where  $m$  is the diffraction order,  $\theta_i$  is the incident angle,  $n$  is the refractive index of the incident medium (which in this case is P3HT:PCBM), and  $\Lambda$  is the periodicity of the grating. The momentum

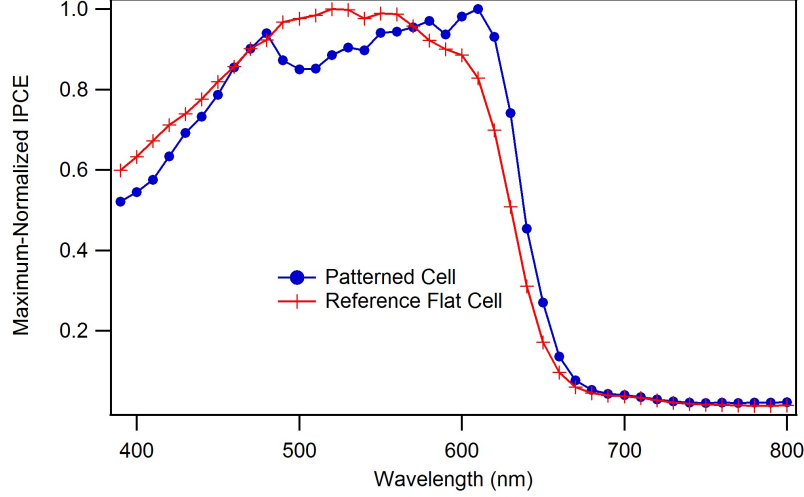


Figure 5.6: Maximum-normalized IPCE curves normalized by their maximum values for a reference cell (red) and a patterned cell (blue).

exchange with a diffraction grating is

$$k_f = k_i + \frac{2\pi m}{\Lambda} \quad (5.1)$$

In order to couple to a surface plasmon, the final momentum must match the plasmon mode.

$$k_{sp} = \frac{2n\pi \sin(\theta_i)}{\lambda} + \frac{2m\pi}{\Lambda} \quad (5.2)$$

The plasmon momentum and  $k_{grating}$  are both constants, so to preserve  $k_{incident}$  under angular variation, the wavelength must redshift. Both absorption and IPCE peaks from possible surface plasmons would redshift with increasing incident angle as well. Figs.5.7 and 5.8 show the maximum-normalized IPCE and simulated optical absorption with incident angle from  $0^\circ$  to  $14^\circ$ . In the absorption, the predicted plasmon peak at 680 nm is visible. Its intensity remains constant over the variation and it shifts wavelength to the red as expected. No other peaks that exhibit a redshift are visible in the absorption

spectrum. The IPCE shows no alteration under angle variation, suggesting that its peaks are not due to the localized electric field generated by surface plasmons.

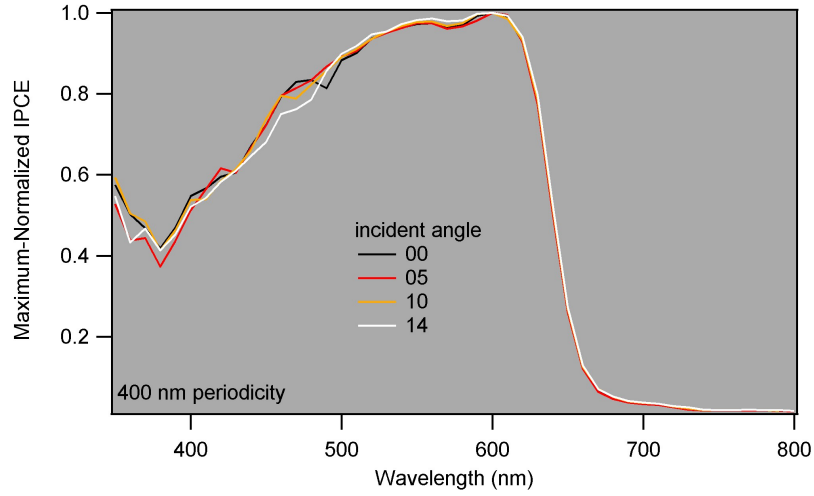


Figure 5.7: Experimental maximum-normalized IPCE vs. wavelength for varying incident angles.

## 5.4 Scattering

Though incident angle variation identifies the plasmonic absorption peak and rules out its contribution to increased efficiency, more characterization is necessary to attribute the IPCE trends to scattering effects. Because the scattering efficiency of the grating is not unity, some of the incident light is scattered, and some of it is reflected in the incident direction and receives no path length alteration. I calculate the diffracted path length as a function of wavelength and refractive index of the active layer. The wavelength with the longest path length will have the most opportunity to be absorbed and create excitons. Eq.5.3 characterizes the change in diffracted path length.

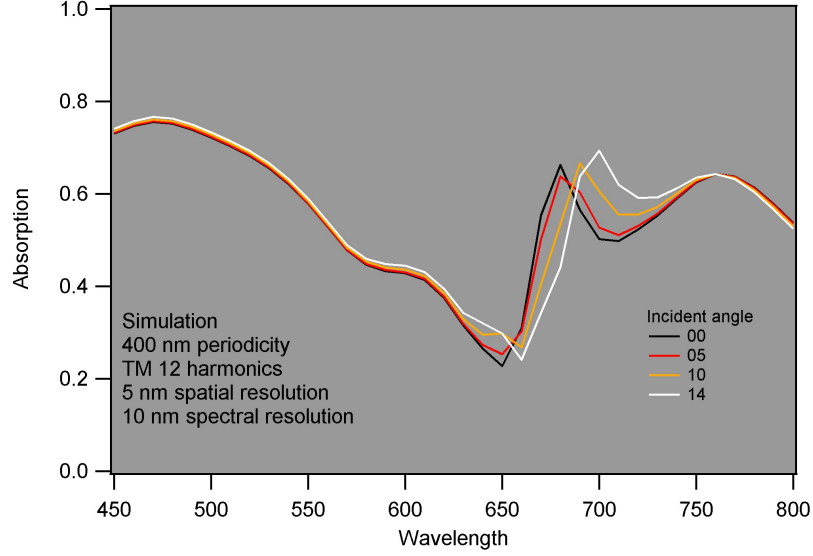


Figure 5.8: Simulated optical absorptions for varying incident angle of an inverted solar cell with the Ag cathode patterned with a 400 nm periodicity diffraction grating.

$$m\lambda = n\Lambda(\sin(\theta_f) - \sin(\theta_i)) \Rightarrow \frac{m\lambda}{n\Lambda} = \sin(\theta_f) - \sin(\theta_i) \quad (5.3)$$

where  $n$  is the refractive index of the P3HT:PCBM. Since  $\frac{m\lambda}{n\Lambda}$  is a constant, the difference between the tangential components of the scattered and incident paths ( $\sin(\theta_f) - \sin(\theta_i)$ ) is invariant with changing incident angle. It is then possible to calculate the length of the scattered path from the normal incidence scattering  $\theta_f = \theta_0$ :

$$l = \sqrt{\frac{t^2}{1 - \sin^2(\theta_0)}} \quad (5.4)$$

where  $l$  is the scattered path length, and  $t$  is the active layer thickness.

Fig.5.10 (right) shows the refractive index of the active layer as a function of the wavelength overlaid with the diffracted path length due to scattering in units of films thickness. The active layer possesses a nonuniform refractive index across the visible that

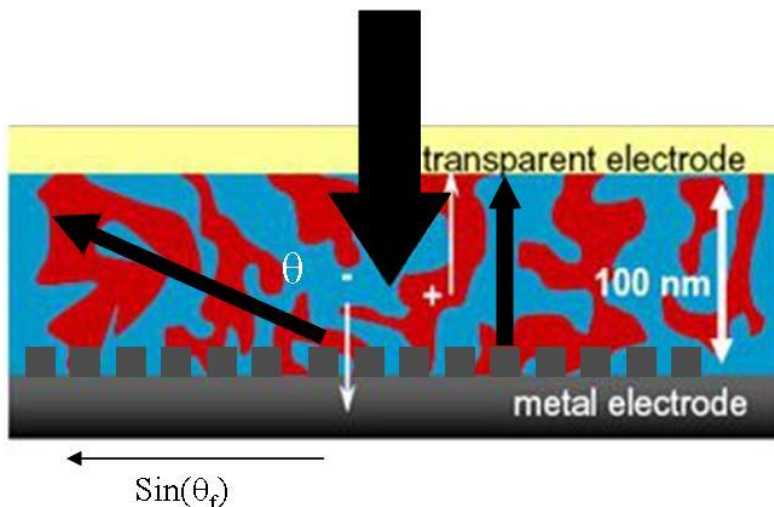


Figure 5.9: Schematic of light scattering from a patterned cathode in a bulk heterojunction organic inverted solar cell.

causes peaks in the path length at 490 nm and 600 nm, matching the IPCE peaks. Though the path length increases in the red, the P3HT:PCBM is not highly absorbing here and the maximum-normalized IPCE shoulder after 600 nm is an example of diminishing return for path length increase.

## 5.5 Conclusions

I have fabricated a patterned organic BHJ solar cell with 400 nm periodicity that generates a surface plasmon at 680 nm at the P3HT:PCBM-Ag interface. This cell has increased electrical performance over its flat counterpart in the form of  $V_{oc}$  and  $J_{sc}$  values of 0.6 V and 9.6 mA/cm<sup>2</sup>. The IPCE curves reveal peaks at 480 nm and 600 nm that do not redshift with increasing incident angle and the 680 nm surface plasmon peak is not visible. The IPCE peaks correspond to the maxima in path length increase due to scattering from the 400 nm grating. In this configuration, there is no plasmonic contribution to the IPCE

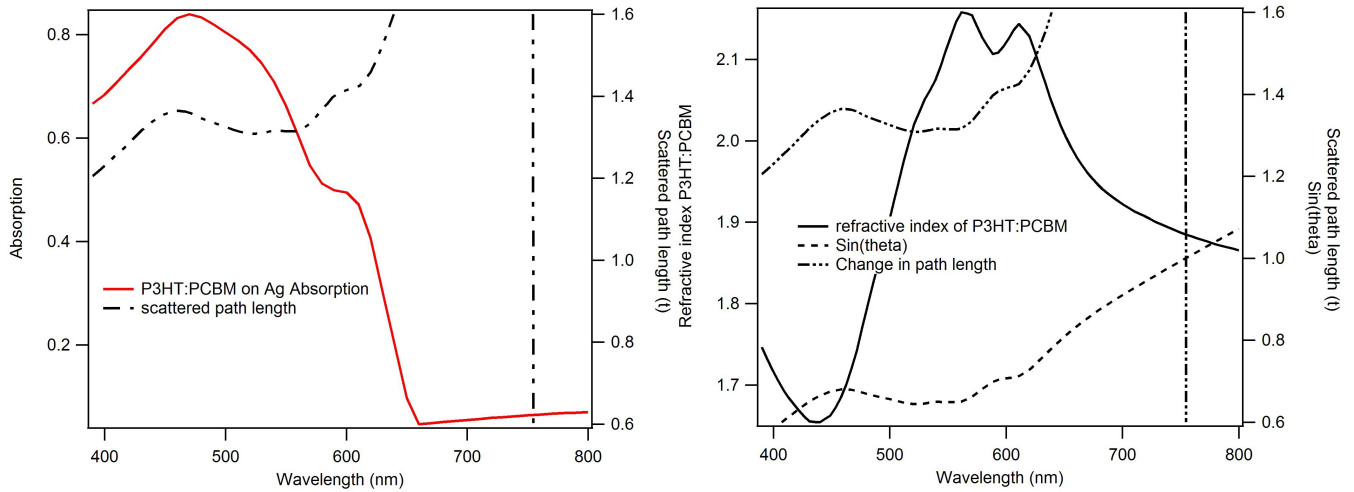


Figure 5.10: Left: Absorption vs. wavelength for a P3HT:PCBM active layer on Ag and the change in path length due to scattering vs. wavelength. Right: Characterization of diffraction behavior as a function of wavelength for a 400 nm periodicity grating in P3HT:PCBM. Shows the real part of the refractive index of P3HT:PCBM (solid line) with  $\text{Sin}(\theta_f)$  (dashed line) that changes the path length of scattered light, and the change in path length (dashed and dotted line).

and the increased electrical performance is solely related to diffraction by the grating.

## APPENDIX A

### RECIPES

#### PLD Recipes:

Ag films

pulse energy: 300 mJ

pulse rate: 40 Hz

target rotation: 20 rpm

substrate rotation: 10 rpm

deposition rate:  $\sim 1$  nm / (1,000 - 2,000) shots

\* note, films thinner than  $\sim 20$  nm cannot be produced as it becomes more energetically favorable the form nanoparticle islands rather than a uniform thin film.

\* if making a Ag-dielectric multilayer metamaterial, the dielectric should be the layer exposed to air to prevent the Ag film from tarnishing.

ZnO thin films

pulse energy: 200 mJ

pulse rate: 25 Hz  
target rotation: 20 rpm  
substrate rotation: 10 rpm  
O<sub>2</sub> pressure: 10 mTorr  
O<sub>2</sub> flow rate: 5 sccm  
substrate temperature: room temperature \*200 ° C  
deposition rate: ~14 nm / (1,000) shots

#### TiO<sub>2</sub> thin films

pulse energy: 200 mJ  
pulse rate: 25 Hz  
target rotation: 20 rpm  
substrate rotation: 10 rpm  
O<sub>2</sub> pressure: 10 mTorr  
O<sub>2</sub> flow rate: 5 sccm  
substrate temperature: room temperature  
deposition rate: ~14 nm / (1,000) shots

#### Al<sub>2</sub>O<sub>3</sub> films

pulse energy: 300 mJ  
pulse rate: 40 Hz  
target rotation: 20 rpm

substrate rotation: 10 rpm

deposition rate:  $\sim 20$  nm / (1,500) shots

## Electron beam recipes

For a  $166.41 \mu\text{m}^2$  exposed area to form a PMMA mask for a deposition of 30 nm Ag on FTO.

1) Clean FTO

sonicate 10 min IPA

sonicate 10 min Acetone

dry with Nitrogen gun

2) Deposit 134 nm PMMA

spincoat 950k, 2 % PMMA in anisol, 45 s, 1000 rpm, 200  $\mu\text{L}$

bake 3 min at 180 °C to remove solvent

3) E-beam exposure to form pattern in PMMA

attach to holder with copper tape

place copper tape on top of film to form contact with target

expose 30 kV,  $170 \mu\text{C} / \text{cm}^2$ , 5.4 pA, 4000 x, 113 s, 0.0061  $\mu\text{m}$  depth in Si

4) Develop pattern

7:3 IPA:DI water mixture for 30 s, agitating lightly

rinse in DI water for 30 s

dry with Nitrogen gun

5) Deposit Ag film

thermally evaporate 30 nm Ag film

6) Liftoff

soak in Acetone at 60 °C for 30 min

spray with a heated Acetone stream to remove Ag.

## Ion beam recipes

Milling into Ag: 400 nm, periodicity arrays, 19 periods circular holes.

30 kV, 48 pA, 12,000 x

Bitmap size: 7.6  $\mu\text{m}$  x 7.6  $\mu\text{m}$ , 400 nm periodicity, 19 periods

Set material to Si

Table A.1: Ion beam milling of Ag

hole diameter	Si depth	time (s)
250 nm	600 $\mu\text{m}$	342
180 nm	700 $\mu\text{m}$	211
150 nm	600 $\mu\text{m}$	127

Milling into a Metamaterial: 4 pair Ag-Al<sub>2</sub>O<sub>3</sub> on glass, oxide on top.

Bitmap size: 7.6  $\mu\text{m}$  x 7.6  $\mu\text{m}$ , 400 nm periodicity, 19 periods

Set material to Si

Table A.2: Ion beam milling of 4 pair MM

hole diameter	Si depth	time (s)
250 nm	100 nm	105
210 nm	70 nm	52
180 nm	70 nm	93
150 nm	70 nm	27
50 nm	300 nm	14

## Spincoating:

520 nm polystyrene beads in a hexagonally close packed monolayer

560 uL PS beads in DI water solution : 80 uL Triton-Methanol solution

spincoat (100 - 300)uL

500 rpm – 330 rpmpm – 5 s

100 rpm – 330 rpmpm – 1 s

1500 rpm – 550 rpmpm – 60s

## PMMA thin films

Table A.3: PMMA Spincoating curves from Meredith Hampton

% PMMA in anisol	rpm	thickness (nm)
10	9000	477
10	8000	508
4	8000	97
4	6000	110
4	4000	139
2.5	1000	128
2.5	1510	104
2.5	2000	96

Table A.4: 950k PMMA Spincoating curves

% PMMA in anisol	rpm	time (s)	volume ( $\mu\text{L}$ )	thickness (nm)
2	600	60	200	173
2	800	60	200	180
2	900	60	200	190
2	1000	60	200	89
2	500	45	400	198
2	600	45	400	173
2	700	45	400	153
2	800	45	400	161
2	900	45	400	135
2	1000	45	200	135
2	800	45	200	+
2	800	45	200	184
2	800	45	200	+ bake
2	800	45	200	292

Table A.5: 495k PMMA Spincoating curves

% PMMA in anisol	rpm	time (s)	volume ( $\mu\text{L}$ )	thickness (nm)
8	8000	60	200	422
8	8000	240	200	420

## APPENDIX B

### POLARIZATION STUDIES THROUGH VARIOUS METAMATERIAL CONFIGURATIONS

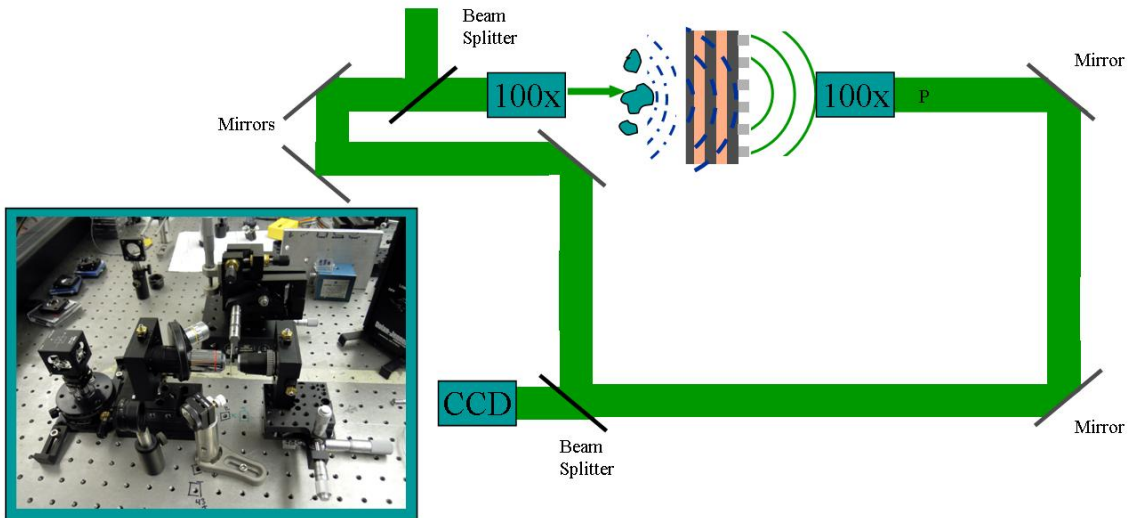


Figure B.1: Schematic of the system used to measure the incident and transmitted polarizations. Inset, a photograph of the sample mount, beamsplitter, and alignment controls.

# Step by Step

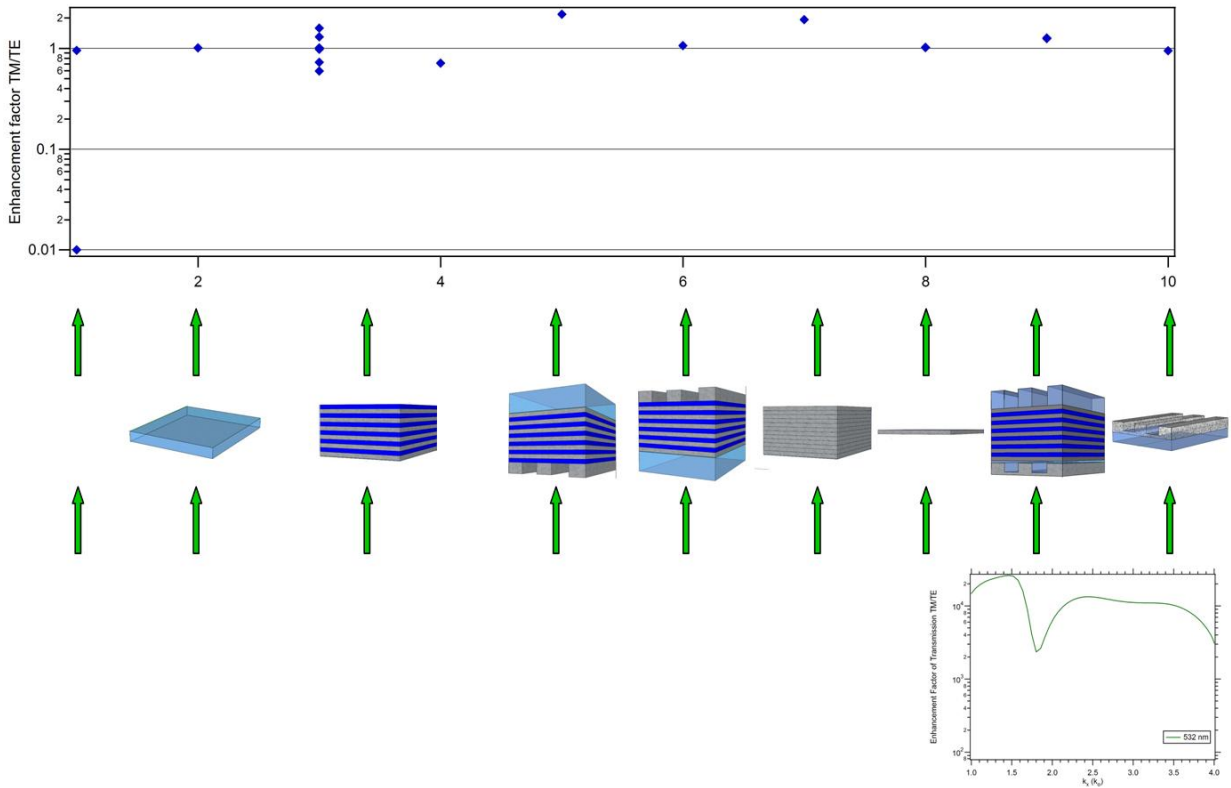


Figure B.2: Polarization enhancement of the TM over TE linear polarizations for various metamaterial configurations. From left to right: the samples measured are air, a glass substrate, an Ag-Al<sub>2</sub>O<sub>3</sub> metamaterial, an Ag plasmonic grating on a metamaterial on glass, a glass substrate on a metamaterial on a plasmonic grating, a thick Ag slab with the same thickness as the metamaterial, a thin Ag slab with thickness equivalent to one layer in the metamaterial, a far-field superlens with a plasmonic grating source on a metamaterial on a plasmonic grating, a plasmonic grating on glass. Below is the simulated TM/TE transmission enhancement for the studied metamaterial at 532 nm incident wavelength.

# Cross Polarization

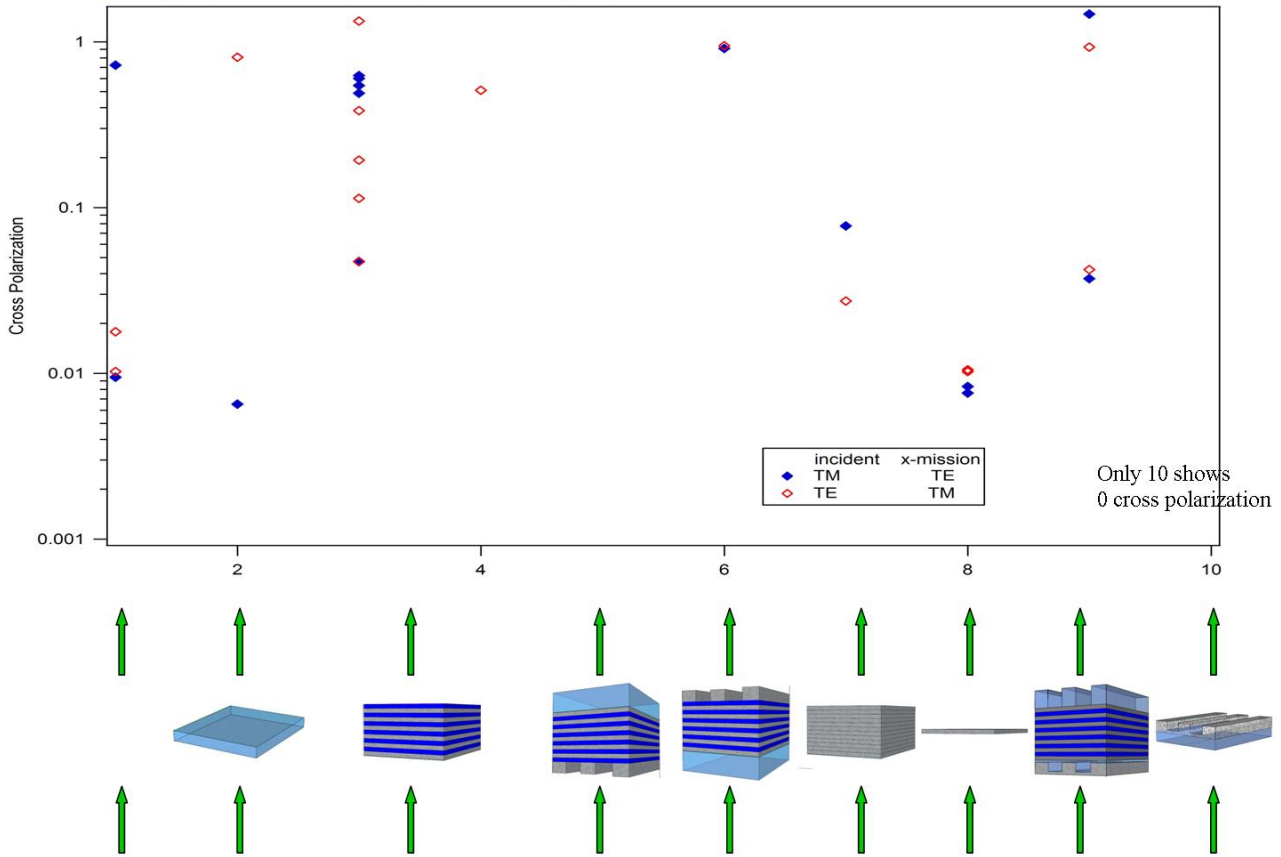


Figure B.3: The cross polarization contrast vs. sample design for various configurations of a metamaterial with graphical representations of the sample. From left to right: the samples measured are air, a glass substrate, an Ag- $\text{Al}_2\text{O}_3$  metamaterial, an Ag plasmonic grating on a metamaterial on glass, a glass substrate on a metamaterial on a plasmonic grating, a thick Ag slab with the same thickness as the metamaterial, a thin Ag slab with thickness equivalent to one layer in the metamaterial, a far-field superlens with a plasmonic grating source on a metamaterial on a plasmonic grating, a plasmonic grating on glass.

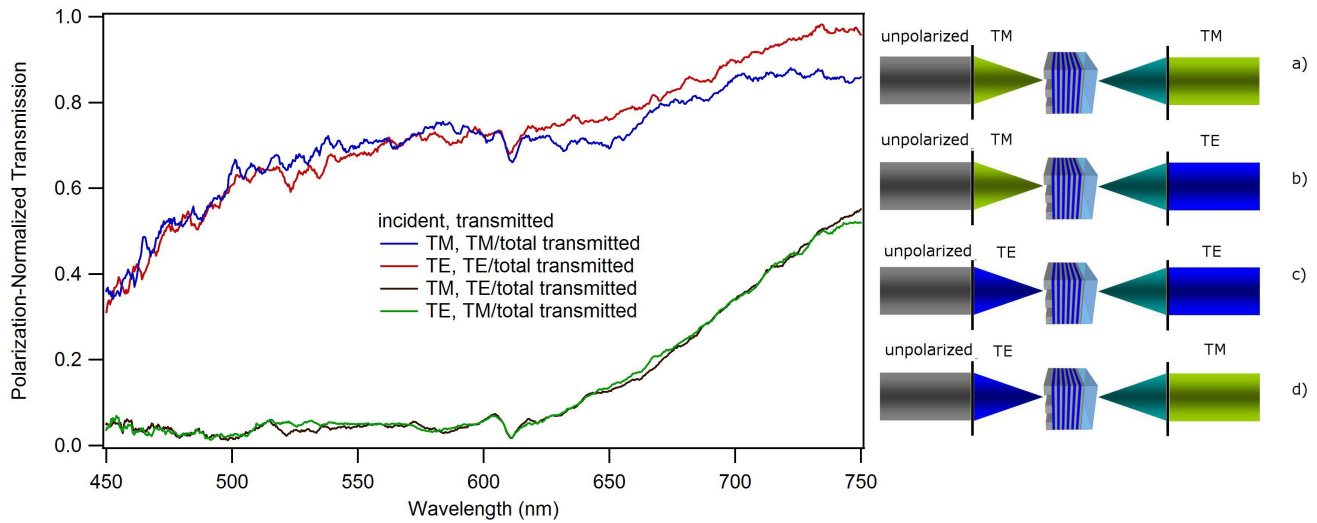


Figure B.4: Left: Transmission enhancement of polarized and unpolarized light through a plasmonic grating and metamaterial. Above are the polarized transmissions normalized by the total transmissions for TM and TE incident waves. Right: Simplified graphical representation of the polarized transmission. In each system, collimated, unpolarized light is linearly polarized and focused through an objective onto the sample, then transmitted light passes through a polarizer and is analyzed with a spectrometer. In a) incident light is TM polarized, measured transmitted light is TM polarized. In b) incident light is TM polarized, collected transmitted light is TE polarized. In c) incident light is TE polarized, collected transmitted light is TE polarized. In d) incident light is TE polarized, collected transmitted light is TM polarized. Images b and d are examples of cross-polarization.

## APPENDIX C

### EXPERIMENTAL SET-UPS

#### **Kretschman-Raether Configuration: (Fig.C.1)**

The Kretschman-Raether set-up was used with the superlens in the visible studies. The incident polarized beam was rotated around the metamaterial located at the eucentric point of the rotation arms. Diffracted orders were detected with a photo diode on a rotating arm at a fixed distance in the far-field. Index matching oil was used to ensure continuous contact of the  $n=1.5$  prism and the metamaterial.

#### **Interference Microscope: (Fig.C.2)**

The interference microscope was built for use with a far-field superlens operating with visible optics. To avoid the overlap of evanescent wave signal and propagating light, the metamaterial was tuned to attenuate the propagating wave. The signal from evanescent waves was collected in the transmission arm, while the information scattered by propa-

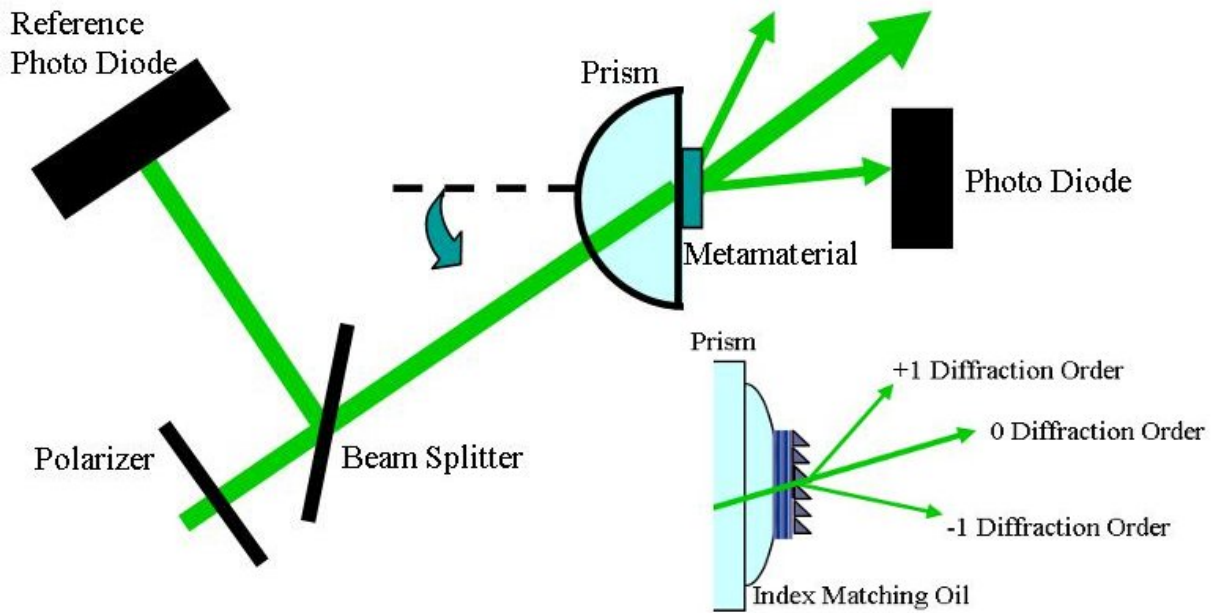


Figure C.1: Schematic of the Kretschman-Raether configuration with inset zoom of the metamaterial-prism interface and diffracted orders.

gating waves was collected in the reflected arm. The two signals could be interfered to form a subdiffraction limited image. The reflected arm path was varied with a micrometer to achieve phase matching of the two beams. It was also used to measure the cross and parallel polarization through various metamaterial configurations.

### Bright-Field Microscope in a Confocal-Like Configuration: (Fig.C.3)

Our Nikon microscope was modified to measure the reflection and transmission with a spectrometer. The single mode incident fiber, iris, and low magnification objective were used to 1) keep the opening angle of the light as small as possible ( $\sim 4^\circ$ ) so that we can keep true normal incidence and 2) focus the incident light on the smallest possible

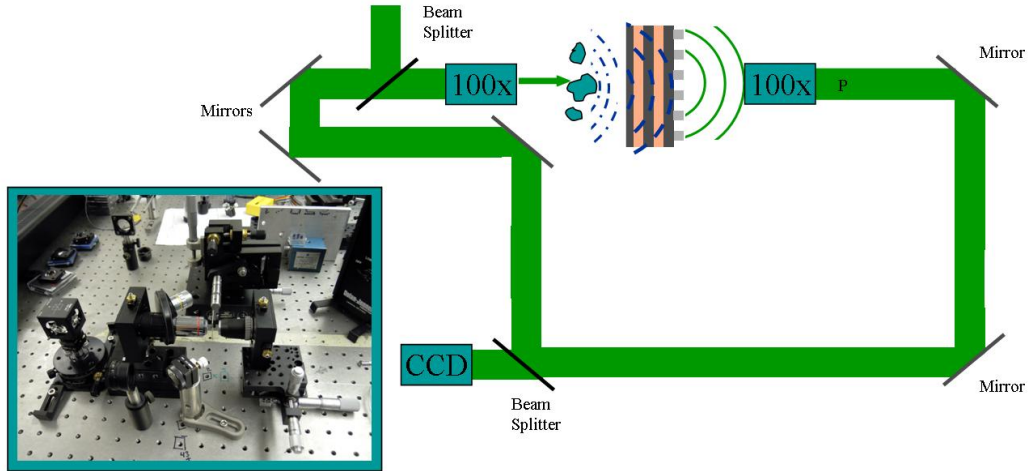


Figure C.2: Schematic of the interference microscope with inset picture of the sample holder with incident and transmitted objectives and positioning mechanisms.

nanostructures without contributions from the surrounding substrate. This microscope was used to measure the reflection and transmission from a single plasmonic diffraction grating on a metamaterial, cross and parallel polarization transmission through a metamaterial, and extraordinary transmission from a hole array in thin films. On the reflected arm, an iris and single mode fiber were used to cut the edges of the signal to measure only the 0 diffracted order from the gratings.

### IPCE With Variable Incident Angle: (Fig.C.4)

This IPCE set-up was used to measure the IPCE vs. wavelength for various incident angles of a patterned and flat inverted organic bulk heterojunction solar cell. The solar cell is mounted at the eucentric point of the incident arm and the reflected arm and a

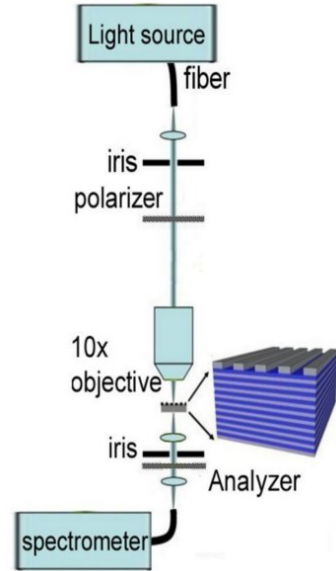
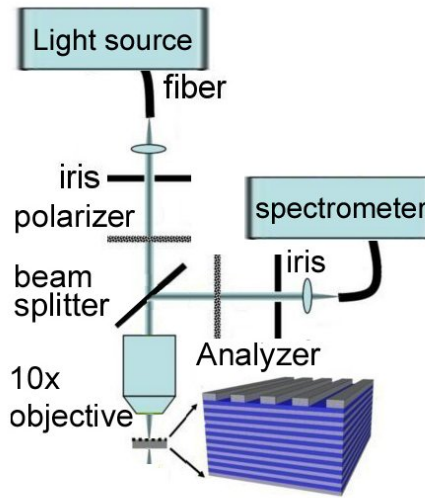
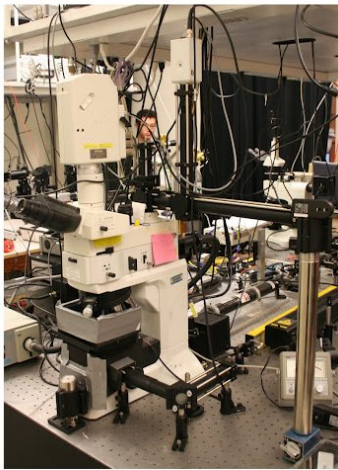


Figure C.3: Left: a photograph of our Nikon microscope modified to measure the reflection and transmission vs. wavelength for a  $15 \mu\text{m}$  spot. Middle: Schematic of the microscope in reflection. Right: Schematic of the microscope in transmission.

physical contact is made between the anode and electrical pins. The incident arm can rotate from  $0$  to  $65^\circ$ . Because the patterned grating is hexagonal it is necessary to have rotation in the  $\phi$  direction to excite surface plasmons along the correct lattice direction. This is achieved by rotating the sample. For reflection studies, the minimum incident angle is limited by the angular size of the detector arms to  $15^\circ$ .

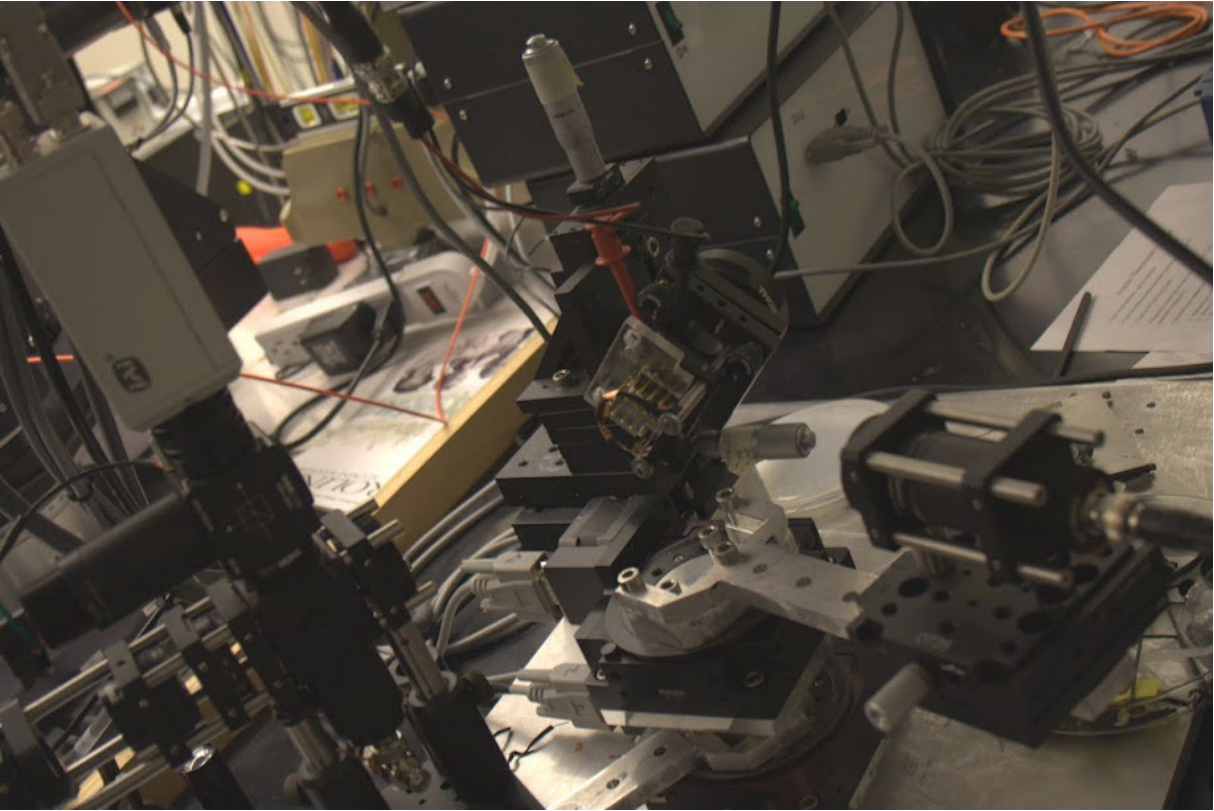


Figure C.4: Photograph of the IPCE set-up with adjustable incident angle.

## BIBLIOGRAPHY

- Abbe, E. (1873). *Mikroskop. Anat.*, 9:413–468.
- Atwater, H. A. and Ablert, P. (2010). Plasmonics for improved photovoltaic devices. *Nature Materials*, 9:205–213.
- Bethe, H. (1944). Theory of Diffraction by Small Holes. *Physical Review*, 66(7-8):163–182.
- Born, M. and Wolf, E. (2002). *Principles of Optics*. Cambridge University Press.
- Cai, W., Dentcho, A. G., and Shalaev, V. M. (2005). Superlens based on metal-dielectric composites. *Physical Review B*, 72:193101.
- Chang, S.-H., Gray, S., and Schatz, G. (2005). Surface plasmon generation and light transmission by isolated nanoholes and arrays of nanoholes in thin metal films. *Optics Express*, 13(8):3150–65.
- Davis, T. J. (2009). Surface plasmon modes in multi-layer thin-films. *Optics Communications*, 282:135–140.
- deCeglia, D., Vincenti, M. A., M, S., Akozbek, N., and Bloemer, M. J. (2011). Plasmonic band edge effects on the transmission properties of metal gratings. *AIP Advances*, 1:032151.
- Degiron, A. and Ebbesen, T. W. (2005). The role of localized surface plasmon modes in the enhanced transmission of periodic subwavelength apertures. *Journal of Optics A*, 7.
- Durant, S., Liu, Z., Steele, J. M., and Zhang, X. (2006). Theory of the transmission properties of an optical far-field superlens for imaging beyond the diffraction limit. *J. Opt. Soc. Am. B*, 23(11):2383–2392.
- Ebbesen, T. W., Lezec, H. J., Ghaemi, H. F., Thio, T., and Wolff, P. A. (1998). Extraordinary optical transmission through sub-wavelength hole arrays. *Nature*, 391(12):667.
- Economou, E. N. (1969). Surface Plasmons in Thin films. *Physical Review*, 182(2):182.
- Fang, N., Lee, H., Sun, C., and Xiang, Z. (2005). Sub-Diffraction-Limited Optical Imaging with a Silver Superlens. *Science*, 308:534–537.
- Ghaemi, H. F., Thio, T., Grupp, D. E., Ebbesen, T. W., and Lezec, H. J. (1998). Surface plasmons enhance optical transmission through subwavelength holes. *Physical Review B*, 58(11):6779–6782.

- Grupp, D. E., Lezec, H. J., Ebbesen, T. W., Pellerin, K. M., and Thio, T. (2000). Crucial role of metal surface in enhanced transmission through subwavelength apertures. *Applied Physics Letters*, 77(11):1569–1571.
- Jacob, Z., Alekseyev, L. V., and Narimanov, E. (2006). Optical Hyperlens : Far-field imaging beyond the diffraction limit. *Optics Express*, 14(18):8247–8256.
- Kim, S. S., Na, S. I., Jo, J., Kim, D. Y., and Nah, Y. C. (2008). Plasmon enhanced performance of organic solar cells using electrodeposited Ag nanoparticles. *Applied Physics Letters*, 93:073307.
- Kim, T. J., Thio, T., Ebbesen, T. W., Grupp, D. E., and Lezec, H. J. (1999). Control of optical transmission through metals perforated with subwavelength hole arrays. *Optics letters*, 24(4):256–8.
- Klein Koerkamp, K., Enoch, S., Segerink, F., van Hulst, N., and Kuipers, L. (2004). 2004 Strong Influence of Hole Shape on Extraordinary Transmission through Periodic Arrays.pdf. *Physical Review Letters*, 92(18):183901.
- Kuhta, N. A., Podolskiy, V. A., and Efros, A. L. (2007). Far-field imaging by a planar lens : Diffraction versus superresolution. *Physical Review B*, 76:205102.
- Kume, T., Hayashi, S., Ohkuma, H., and Yamamoto, K. (1995). Enhancement of photoelectric conversion efficiency in copper phthalocyanine solar cell: white light excitation of surface plasmon polaritons. *Japan Journal of Applied Physics*, 34:6448–6451.
- Lezec, H. J., Pellerin, K. M., Thio, T., Pendry, J. B., and Ebbesen, T. W. (2001). Theory of Extraordinary Optical Transmission through Subwavelength Hole Arrays. *Physical Review Letters*, 86(6):1114.
- Lindquist, N. C., Luhman, W. A., Oh, S. H., and Holmes, R. J. (2008). Plasmonic nanocavity arrays for enhanced efficiency in organic photovoltaic cells. *Applied Physics Letters*, 93:123308.
- Liu, Z. (2007). Far-Field Optical Hyperlens Magnifying. *Science*, 315:1686.
- Liu, Z., Durant, S., Lee, H., Pikus, Y., Xiong, Y., Sun, C., Zhang, X., and X (2007). Far-field optical superlens. *Nano. Lett.*, 7(2):403–408.
- Liu, Z., Fang, N., Yen, T.-j., and Zhang, X. (2003). Rapid growth of evanescent wave by a silver superlens. *Applied Physics Letters*, 83(25):5184–5186.
- Melville, D. O. S. and Blaikie, R. J. (2005). Super-resolution imaging through a planar silver layer. *Optics Express*, 13(6):2127–2134.
- Min, C., Li, J., Veronis, G., Lee, J.-Y., Fan, S., and Peumans, P. (2010). Enhancement of optical absorption in thin-film organic solar cells through the excitation of plasmonic modes in metallic gratings. *Applied Physics Letters*, 96:133302.

- Morfa, A. J., Rowlen, K. L., Reilly, T. H., Romero, M. J., and Van de Lagemaat, J. (2008). Plasmon-enhanced solar energy conversion in organic bulk heterojunction photovoltaics. *Applied Physics Letters*, 92:013504.
- Na, S.-I., Kim, S.-S., Jo, J., Oh, S.-H., Kim, J., and Kim, D.-Y. (2008). Trapping light in organic plastic solar cells with integrated diffraction grating. *Advanced Functional Materials*, 18:3956–3963.
- Niggemann, M., Glatthaar, M., Gombert, A., Hinsch, A., and Wittwer, V. (2004). Diffraction gratings and buried nano-electrodes – architectures for organic solar cells. *Thin Solid Films*, 451-452:619–623.
- Palik, E. D. (1985). *Handbook of Optical Constants*. Academic Press Limited.
- Pendry, J. B. (2000). Negative Refraction Makes a Perfect Lens. *Physical Review Letters*, 85(18):3966.
- Perez-Lombard, L., Ortiz, J., and Pout, C. (2008). A review on buildings energy consumption information. *Energy and Buildings*, 40:394–398.
- Ramakrishna, S. A., Pendry, J. B., K, W. M. C., and J, S. W. (2003). Imaging the near field. *Journal of Modern Optics*, 50(9):1419–1430.
- Ray, E. and Lopez, R. (2011). Numerical design and scattering losses of a one-dimensional metallo-dielectric multilayers with broadband coupling of propagating waves to plasmon modes in the visible range. *J Opt Soc Am B*, 28:1778–1781.
- Rolland, J. P., Maynor, B. W., Euliss, L. E., Exner, A. E., Denison, G. M., Desimone, J. M., and Nanobiomaterials, S.-s. (2005). Direct Fabrication and Harvesting of Monodisperse , Shape-Specific Nanobiomaterials. *J Am chem Soc*, 127(28):10096.
- Salandrino, A. and Engheta, N. (2006). Far-field subdiffraction optical microscopy using metamaterial crystals: Theory and simulations. *Physical Review B*, 74:075103.
- Smith, D. R. and Schurig, D. (2003). Electromagnetic Wave Propagation in Media with Indefinite Permittivity and Permeability Tensors. *Phys. Rev. Lett.*, 90077405.
- SuperManu (2007). Onde electromagnetique. *Wikipedia*, [http://en.wikipedia.org/wiki/Electromagnetic\\_radiation](http://en.wikipedia.org/wiki/Electromagnetic_radiation).
- Tikhodeev, S. G., Yablinskii, A. L., Muljarov, E. A., Gippius, N. A., and Ishihara, T. (2002). Quasiguidded modes and optical properties of photonic crystal slabs. *Physical Review B*, 66:045102.
- Tomita, S., Yokoyama, T., Yanagi, H., Wood, B., Pendry, J. B., Fujii, M., and Hayashi, S. (2008). Resonant photon tunneling via surface plasmon polaritons through metamaterials. *Optics Express*, 16(13):9942.

- Tretyakov, S. (2000). *Analytical Modeling in Applied Electromagnetics*. Artech House, Inc.
- Tvingstedt, K., Persson, N.-K., and Inganäs, O. (2007). Surface plasmon increase absorption in polymer photovoltaic cells. *Applied Physics Letters*, 91:113514.
- van der Molen, K., Klein Koerkamp, K., Enoch, S., Segerink, F., van Hulst, N., and Kuipers, L. (2005). Role of shape and localized resonances in extraordinary transmission through periodic arrays of subwavelength holes: Experiment and theory. *Physical Review B*, 72(4):045421.
- Wang, C., Gan, D., Zhao, Y., Du, C., and Luo, X. (2008a). Demagnifying super resolution imaging based on surface plasmon structures. *Optics Express*, 16(8):5427–5434.
- Wang, C., Zhao, Y., Gan, D., Du, C., and Luo, X. (2008b). Subwavelength imaging with anisotropic structure comprising alternately layered metal and dielectric films. *Optics Express*, 16(6):4217.
- Wang, D. H., Choi, D.-G., Lee, K.-J., Jeong, J.-H., Jeon, S. H., Park, O. O., and Park, J. H. (2010). Effect of the ordered 2D-dot nano-patterned anode for polymer solar cells. *Organic Electronics*, 11:285–290.
- Wood, B., Pendry, J. B., and Tsai, D. P. (2006). Directed subwavelength imaging using a layered metal-dielectric system. *Physical Review B*, 74:115116.
- Xiong, Y., Liu, Z., Durant, S., Lee, H., Sun, C., and Zhang, X. (2007a). Tuning the far-field superlens : from UV to visible. *Optics Express*, 15(12):7095–7102.
- Xiong, Y., Liu, Z., Sun, C., and Zhang, X. (2007b). Two-Dimensional Imaging by Far-Field Superlens at Visible Wavelengths. *Nano Letters*, 7(11):3360.
- Yang, Z. Y. and Lu, Y. F. (2007). Broadband nanowire-grid polarizers in ultraviolet-visible-near-infrared regions. *Optics express*, 15(15):9510–9.
- Zhang, Z., Du, J., Guo, X., and Luo, X. (2007). High-efficiency transmission of nanoscale information by surface plasmon. *Journal of Applied Physics*, 102:074301.
- Zhao, Y., Gan, D., Cui, J., Wang, C., Du, C., and Luo, X. (2008). Super resolution imaging by compensating oblique lens with metallodielectric films. *Optics Express*, 16(8):5697–5707.